IEEE Access
Multidisciplinary | Rapid Review | Open Access Journal

Received 11 December 2023, accepted 30 December 2023, date of publication 2 January 2024, date of current version 2 February 2024.

Digital Object Identifier 10.1109/ACCESS.2023.3349275

RESEARCH ARTICLE

Multiple Quantum Barrier Avalanche Photodiode Based on GaN/AlGaN Heterostructures for Long Wavelength Infrared Detection

SOMRITA GHOSH[1], ARITRA ACHARYYA[2], ARINDAM BISWAS[1,3], AMIT BANERJEE[4], HIROSHI INOKAWA[5], (Member, IEEE), HIROAKI SATOH[5], (Member, IEEE), ALEXEY Y. SETEIKIN[6,7], AND I. G. SAMUSEV[6]

[1]Department of Mining Engineering, Kazi Nazrul University, Burdwan, Asansol, West Bengal 713340, India
[2]Department of Electronics and Communication Engineering, Cooch Behar Government Engineering College, Harinchawra, Ghughumari, Cooch Behar, West Bengal 736170, India
[3]Centre for IoT and AI Integration with Education-Industry-Agriculture, Kazi Nazrul University, Burdwan, Asansol, West Bengal 713340, India
[4]Microsystem Design-Integration Laboratory, Department of Physics, Bidhan Chandra College, Asansol, West Bengal 713303, India
[5]Research Institute of Electronics, Shizuoka University, Hamamatsu 4328011, Japan
[6]Research and Education Center for Laser Nanotechnology and Information Biophysics, Immanuel Kant Baltic Federal University, 236000 Kaliningrad, Russia
[7]Computation Biophysics Group, Amur State University, 675027 Blagoveshchensk, Russia

Corresponding authors: Arindam Biswas (mailarindambiswas@yahoo.co.in), Aritra Acharyya (ari_besu@yahoo.co.in), and I. G. Samusev (is.cranz@gmail.com)

This work was supported in part by the Japan–India Science Cooperative Program between Japan Society for the Promotion of Science (JSPS) and Department of Science and Technology (DST) under Grant JPJSBP120207708 (Japan) and Grant DST/INT/JNPS/P-310/2020 (India); in part by the 2023 Cooperative Research Project on Biomedical Engineering, funded by the Research Centre for Biomedical Engineering, Japan in association with Research Institute of Electronics (RIE), Shizuoka University, Japan, under Project 2055; and in part by the Device Development Programme by the Department of Science Technology, Ministry of Science and Technology, Government of India, under Grant DST/TDT/DDP-38/2021.

ABSTRACT A multiple quantum barrier (MQB) avalanche photodiode (APD) structure based on GaN/$Al_xGa_{1-x}N$ material system has been proposed in this paper which is capable of detecting infrared (IR) signal up to 6.0 μm wavelength. A self-consistent quantum drift-diffusion (SCQDD) model developed by the authors, has been used to determine the current-voltage characteristics under dark and illuminated conditions, spectral response, excess noise properties, signal-to-noise ratio, time and frequency responses. Results show that the proposed MQB APD attains peak responsivity of 60 AW^{-1} at 3.0 μm wavelength. Incorporation of a dedicated thin *n*-type GaN layer for avalanche multiplication in between the p^+-GaN contact layer and MQB constant-field drift-layer ensures significantly low noise equivalent power under normal operating conditions at room temperature (300 K). Optical pulse response of the device reveals that special restriction over the charge multiplication able to supress the minor peaks of the current response and consequently significantly narrow pulse response can be achieved. Narrow pulse response leads to broad bandwidth of 274.5 GHz, which is significantly broader than the existing IR photo-detectors.

INDEX TERMS Avalanche photodiodes, multiple quantum barrier, self-consistent quantum drift-diffusion model, infrared, heterojunction, responsivity, pulse response, bandwidth.

I. INTRODUCTION

Avalanche photodiodes (APDs) are most suitable optical detector for the optical receivers in long-haul optical communication systems [1]. The APDs are preferred as optical signal detector over other photo-detectors in both free space and fibre-optic communication systems, except the applications in which the signal-to-noise ratio (SNR)-budget is low. In those cases, low noise *p-i-n* detector, in combination with the trans-impedance amplifier are preferred. However, high internal gain mechanism of APDs eliminates the burden of trans-impedance amplifiers in case of the applications where SNR-budget is not a major concern. Moreover, high sensitivity and ultra-high speed of APD are

The associate editor coordinating the review of this manuscript and approving it for publication was Shuo Sun.

the primary reasons behind the superiority of APDs over other photo-detectors [2], [3], [4], [5], [6]. The APD-based optical receivers can achieve high signal-to-noise ratio within smallest noise equivalent power among all state-of-the-art photo detectors [7]. APDs are most suitable for the detection of very weak ultra-high speed optical signals. Moreover, other than optical communication systems, APDs are also used in various applications like bio-medical engineering, scintillation detection of nuclear radiation, particle detection, optical ranging, astronomical observations, material analysis, military applications, etc. The Silicon (Si) based APDs are most commonly used in various visible wavelength and short-infrared wavelength (e.g., 850, 905, 940 nm) optical signal detection and 850 nm fibre-optic communication due to the lower cost and matured technology of Si [8], [9], [10], [11], [12], [13], [14], [15], [16], [17].

Dark current is the most important factor which determine the sensitivity of the APDs. The Si APD of 3.0 mm diameter produces minimum dark current of 10 nA at room temperature (300K), which can be further reduces to 0.1 nA at –40° C with appropriate cryogenic cooling arrangements [18]. However, some important applications like deep space astronomical observations, composite material analysis, etc., demand very weak signal detection capability (high responsivity over broader range from ultra-violet (UV) spectrum to mid-infrared spectrum). Modern day ultra-high speed, long-haul optical communication systems require ultra-narrow impulse response of the optical detectors. These requirements can be fulfilled by ordinary Si APDs. Scaling of the device dimensions in nano scale, the Si APDs (nano-APDs) can fulfil the requirements associated with the ultra-high speed signal detection; but due to the narrow bandgap of Si (E_g = 1.12 eV at 300 K) dark current of Si nano-APDs rises extensively due to large amount of band-to-band tunnelling at room temperature. As a result of that its signal to noise ratio (SNR) deteriorated and Si nano-APDs remain no longer suitable for weak optical detection. In the year of 2017, Acharyya et al. proposed the use of multi-quantum well (MQW) or multi-quantum barrier (MQB) structures in p^+-i_{MQB}-n^+ structured APDs for supressing the dark current below nA range, even if the dimensions of the device are scaled down to nm range. They further developed the self-consistent quantum drift-diffusion (SCQDD) model for analysing the spectral response, excess noise properties, time and frequency responses of MQW/MQB APDs. They have shown that the MQB nano-APDs, based on Si∼3C-SiC material system, are most suitable for aforementioned applications demanding very low dark current, high responsivity over broad wavelength range, ultra-high speed, and broad bandwidth. The numerical simulation results are validated by comparing those with the experimental data available in literature [19].

In the present paper the authors have proposed a p^+-n-i_{MQB}-n^+ nano-APD structure, based on GaN/Al_xGa_{1-x}N material system in order to achieve lower dark current, higher responsivity over broader wavelength range, better noise characteristics and better time and frequency responses as compared to the earlier proposed MQB APDs based on Si/3C-SiC heterojunctions. The device structure and possible fabrication steps are briefly discussed in this paper. The effects spontaneous and piezoelectric polarization in GaN and AlGaN layers have been incorporated in the earlier developed SCQDD model, and the modified SCQDD model has been used to study the spectral response, excess noise parameters, time and frequency responses of the proposed APDs structure and the results are presented through appropriate graphs and tables with detailed discussions. Finally, the simulation results are validated by comparing those with the experimental data available in literature. A comparative study has been presented at the end of the paper between the proposed device and other commercially available photodetectors in order to establish the superiority of the proposed device.

II. DEVICE STRUCTURE AND FABRICATION

The cross-sectional structure diagram and top view of the GaN/$Al_{0.3}Ga_{0.7}$N/GaN MQB APD are shown in Figure 1 (a) and (b). Here, the Al mole fraction $x = 0.3$ in $Al_xGa_{1-x}N$ has been chosen. The important device dimensions are listed in Table 1. The fabrication technology employed in creating the MQB APD structure depicted in Figure 1 (a) plays a crucial role in attaining optimal device performance, specifically enhancing spectral response and signal-to-noise ratio (SNR). Notably, defects and dislocations introduced during etching steps can elevate dark current and compromise the SNR of the device. Therefore, careful consideration must be given to the technology chosen for fabricating the GaN/$Al_{0.3}Ga_{0.7}$N/GaN MQB MQB APD. In this context, two potential process technologies have been discussed, hinging on (i) the molecular beam epitaxy (MBE) growth technique and (ii) the metal-organic chemical vapor deposition (MOCVD) technique. Between these two options, the latter—MOCVD-based device fabrication—proves superior in achieving enhanced device performance, characterized by lower dark current, and improved spectral response and SNR [20].

A. METHOD – 1

The initial substance for growing the MQB APD structure is a 400 μm thick, 4-inch diameter single-polished n^+-GaN substrate. The n-type doping concentration of the n^+-GaN substrate is $2.0 \times 10^{24} m^{-3}$. The AlGaN/GaN/AlGaN quantum wells can be grown by using molecular beam epitaxy (MBE) technique on the n^+-GaN substrate along (0001) direction. At first a very thin (around 10 nm thick) AlN nucleation layer must be grown on the n^+-GaN substrate at around 800°C temperature. After that the substrate temperature must be reduced to 720°C for growing a 500 nm thick $Al_{0.3}Ga_{0.7}N$ buffer layer doped with n-type Si dopant of dosage 2.0×10^{25} m^{-3}. This buffer layer reduces the growth stress and also used for forming the cathode contact. Next, 9 – 10 cycles of $Al_{0.3}Ga_{0.7}N$/GaN/$Al_{0.3}Ga_{0.7}N$ quantum wells are to be grown on the $Al_{0.3}Ga_{0.7}N$ buffer layer. The thickness

TABLE 1. Dimensions of the structural parameters.

Parameter	Description	Value
L_{ow}	Length of the Optical Window	300 μm
W_{ow}	Width of the Optical Window	300 μm
L_a	Length of the Anode Layer	500 μm
W_a	Width of the Anode Layer	500 μm
L_d	Device Length	1000 μm
W_d	Device Width	1000 μm
L_g	Separation between Anode and Cathode	50 μm
L_c	Length of the Cathode Layer	200 μm
$A_a = (L_aW_a - L_{ow}W_{ow})$	Area of the Anode Layer	1.6×10^4 μm^2
$A_c = (W_dL_c)$	Area of the Cathode Layer	2.0×10^5 μm^2

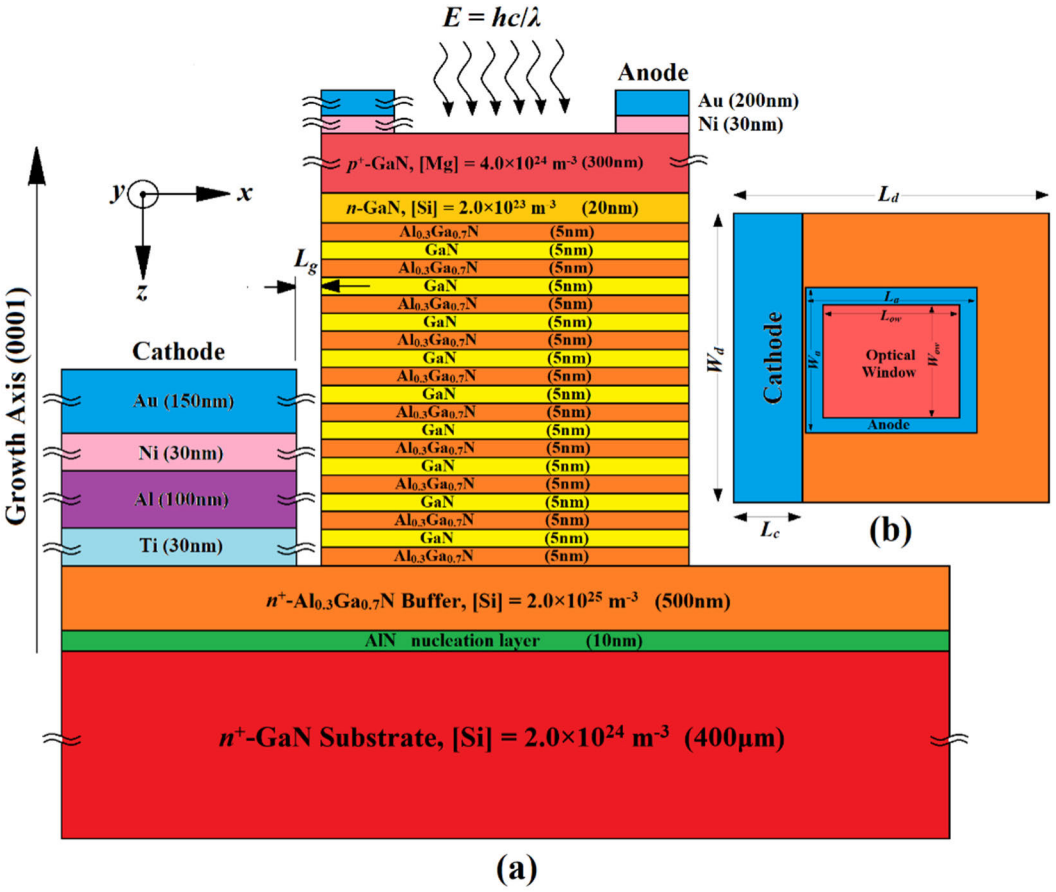

FIGURE 1. (a) Structure diagram of the GaN/$Al_{0.3}Ga_{0.7}N$/GaN Multiple Quantum Barrier avalanche photodiode for infrared detection. (b) Top view of the device structure.

of GaN well and $Al_{0.3}Ga_{0.7}N$ barrier layers are 5 nm. Both the $Al_{0.3}Ga_{0.7}N$ and GaN layers are doped with *n*-type Si dopants of dosage 10^{21} m^{-3}. Finally, a *n*-GaN layer of 20 nm thickness is grown over the final $Al_{0.3}Ga_{0.7}N$ barrier layer. The *n*-GaN layer is kept comparatively highly doped as compared to the $Al_{0.3}Ga_{0.7}N$/GaN/$Al_{0.3}Ga_{0.7}N$ cycles (doped with *n*-type Si dopants of dosage 2.0×10^{23} m^{-3}), in order to form a high-low (hi-lo) density profile of the active layer of the device. The hi-lo doping profile helps to constrict the charge multiplication process within a narrow region and consequently reduces the effective avalanche zone under reverse bias. Finally, the p^+-GaN layer of thickness 300 nm must be grown on the *n*-GaN layer in order to form the p^+-*n* junction. The *p*-type doping can be achieved by using Mg dopants and doping concentration of the p^+-GaN must be kept around 4.0×10^{24} m^{-3}. Therefore, p^+-*n*-i_{MQB}-n^+ structured APD gets its final form. After getting the final p^+-*n*-i_{MQB}-n^+ structure, SiO_2 hard masking, electron beam lithography and Cl_2-based inductively coupled plasma reactive ion etching (ICP-RIE) with moderate etching rate can be used to etch

around 415 nm GaN and AlGaN layers to get the diode mesa structure as shown in Figure 1 (a). After another lithography step followed by vacuum evaporation of Ni(30nm) and Au(200nm) can be used to form the square shaped ring type anode contact layer over the p^+-GaN layer. The optical window size (see Figure 1 (b)) is $L_{ow} \times W_{ow} = 300\mu\text{m} \times 300\ \mu\text{m}$. Finally, the third lithography step followed by the thermal evaporation of Ti (30nm), Al (100nm), Ni (30nm) and Au (150nm) can be used to form the cathode ohmic contact over the n^+-$Al_{0.3}Ga_{0.7}N$ buffer layer.

B. METHOD – 2

In this approach, MQB APDs are grown on a 400nm thick, 4-inch diameter single-polished n^+-GaN substrate. The high-temperature MOCVD system is employed to grow the devices on the n^+-GaN substrate along the (0001)-direction. Trimethyl aluminium (TMAl), trimethyl gallium (TMGa), and ammonia (NH_3) serve as precursors for Al, Ga, and N, respectively, with hydrogen (H_2) chosen as the carrier gas. Si and Mg dopants are used for n- and p-doping of the epi-layers, with silicane (SiH_4) and bis-cyclopentadienyl magnesium (Cp_2Mg) serving as the doping sources, respectively. To enhance the quality of the active layers, an initial very thin (∼100nm) AlN nucleation layer is grown on the n^+-GaN substrate at 1300°C. Subsequently, the substrate temperature is reduced to 1180°C, and a 500nm thick Si-doped $Al_{0.30}Ga_{0.70}N$-buffer layer (dosage: 2.0×10^{25} m^{-3}) is grown on the AlN layer to alleviate growth stress. Following this, 9 – 10 cycles of Si-doped (dosage: 10^{21} m^{-3}) $Al_{0.30}Ga_{0.70}N$/GaN/$Al_{0.30}Ga_{0.70}N$ quantum wells are grown on the $Al_{0.30}Ga_{0.70}N$-buffer layer. To achieve a hi-lo doping profile of the active layer of the device, a Si-doped (dosage: 2.0×10^{23} m^{-3}), 20nm thick n-GaN layer is grown on the final $Al_{0.30}Ga_{0.70}N$-barrier layer. The advantage of the hi-lo doping profile is previously mentioned in the method – 1. Finally, the growth temperature is reduced to 1080°C, and the Mg-doped (dosage: 4.0×10^{24} m^{-3}), 300nm thick p^+-GaN anode contact layer is grown. Upon completion of the p^+-n-i_{MQB}-n^+ structure growth, the entire structure undergoes *ex-situ* thermal annealing under N_2 environment at 900°C to activate the Mg acceptors in the p^+-GaN contact layer. Next, a SiO_2 mask layer is applied to the wafers using plasma-enhanced chemical vapor deposition. The device pattern is then transferred to the mask layer through standard photolithography and reactive ion etching (RIE) processes. Subsequently, the wafers undergo etching inside an inductive coupling plasma etching system with a depth of approximately 415 nm, revealing the n-$Al_{0.30}Ga_{0.70}N$-buffer layer, as illustrated in Figure 1 (a). Following the removal of the residual SiO_2 mask using a buffered oxide etching solution, the wafers are subjected to a 10% NaOH solution at 80°C for 10 minutes to passivate the etching defects on the mesa sidewall. The next step involves transferring the n-electrode (cathode) pattern to the wafer via photolithography, followed by the deposition of a Ti(30nm)/Al(100nm)/Ni(30nm)/Au(150nm) electrode using e-beam and thermal evaporation. Subsequent to lift-off, the n-electrode undergoes rapid annealing at 600°C for 30 seconds in N_2 environment to establish Ohmic contact. Similarly, the p-electrode (anode), composed of Ni(50nm)/Au(200nm), is deposited on the mesa using the same processes. After lift-off, the p-electrode undergoes annealing at 550°C for 5 minutes in N_2 to form Ohmic contact. Finally, a SiO_2 passivation layer is deposited on the wafers to passivate dangling bonds, thereby reducing leakage current. The SiO_2 layer on electrodes is subsequently removed by reactive ion etching (RIE) for performance testing.

In this work, the characterizations of the device have not been presented. Conducting a comprehensive material characterization of the entire device structure is crucial to assess the crystal quality of the fabricated structure. The estimation of Al content and crystal quality of the epilayers can be achieved through the utilization of a high-resolution X-ray diffractometer (Brucker D8 DISCOVER). For an in-depth investigation of the device cross-section, particularly the multi-quantum well (MQW) region, a high-resolution scanning transmission electron microscope (HR-STEM) should be employed. The mesa and electrodes of the detectors can be observed using an optical microscope (Nikon ECLIPSE LV15ONA). To measure the current-voltage (I-V) curves, the PDA FS-Pro 380 semiconductor analyzer can be employed. Detailed results of the full-structure device characterization will be reported in a forthcoming presentation.

III. MODELLING AND SIMULATION

The one-dimensional (1)-D) model of the p^+-n-i_{MQB}-n^+ structured MQB APD based on GaN/$Al_{0.3}Ga_{0.7}N$ material system is shown in Figure 2. Under reverse bias, the highly doped p^+-GaN layer injects electrons into the n-GaN layer. The majority of charge multiplication phenomenon occurs within the high-field n-GaN layer and consequently huge number of electrons entered to the constant field (nearly undoped) MQB drift region (see the simulated electric field profile shown in Figure 2). Therefore, MQB drift-layer does not take part in avalanche multiplication process. As a result of that under optical illumination condition (i.e., when time-varying photon flux density $\Phi^{(\lambda)}(t)$ of wavelength λ is incident on p^+-GaN surface), the wavelengths associated with GaN ($E_g \approx 3.4$ eV at 300 K) are absorbed in p^+- and n-GaN regions and get the chance of being multiplied through the avalanche multiplication at n-GaN layer. Therefore, shorter wavelength (UV spectrum) gets the optical gain from avalanche multiplication. However, the longer wavelengths are absorbed at MQB drift-layer due to the inter sub-band transitions in the quantum wells. Several cycles of quantum wells are responsible for obtaining the sufficiently high optical gain at longer wavelengths (IR-spectrum).

A self-consistent quantum drift-diffusion (SCQDD) model developed by the authors has been used to calculate the multiplied responsivity of the MQB APD structure under reverse bias [19], [21]. The SCQDD model has been formulated by coupling the classical drift diffusion (CLDD) equations with the time-independent Schrodinger's equations associ-

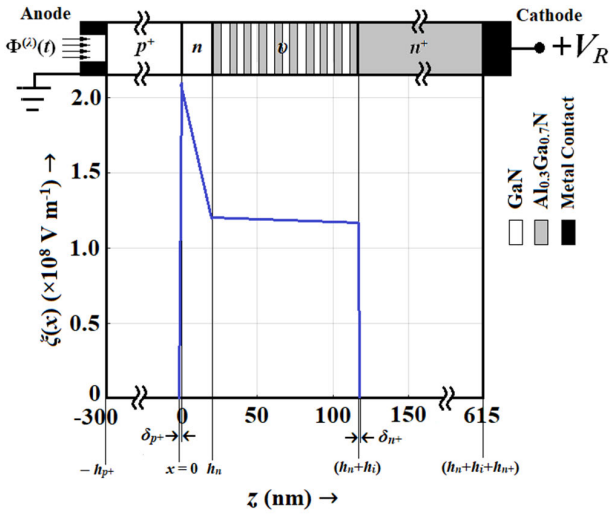

FIGURE 2. One-dimensional model of the GaN/$Al_{0.3}Ga_{0.7}N$ MQB APD and simulated electric field profile (blue lines) under reverse bias. The electric field profile is presented here for the reverse bias of 10.2 V under the dark condition ($\Phi_0^{(\lambda)} = 0$); electric field penetration depths in p^+- and n^+-layers are found to be $\delta_{p+} = 5.46$ nm and $\delta_{p+} = 0.68$ nm respectively.

ated with electrons in conduction band and holes in valance band [21]. The CLDD equations are as follows:

Poisson's Equation:

$$\frac{d}{dz}\left(-\epsilon\frac{dV}{dz} + P_t\right) = q\left(\gamma_p p - \gamma_n n + N\right), \tag{1}$$

Steady-State Continuity Equations:

$$\frac{dJ_r^{(total)}}{dz} = \pm q\left(\sum\nolimits_{\Xi\in\{AV,BBT,TAT\}} G_{r(\Xi)} - R_r\right), \tag{2}$$

Current Density Equations:

$$J_r^{(total)} = -q\left\{\gamma_r r\mu_r \pm D_r\frac{d\left(\gamma_r r\right)}{dz}\right\} + J_{r(opt)}^{(total)}, \tag{3}$$

where $q = 1.6 \times 10^{-19}$ C is the unit electronic charge, space-dependent parameters like $r \in \{p, n\}$ are the hole and electron concentrations, $G_{r(\Xi)}$ are hole and electron generation rates due to avalanche multiplication ($\Xi \equiv$ AV), band-to-band tunneling ($\Xi \equiv$ BBT) and trap-assisted tunneling ($\Xi \equiv$ TAT), R_r are the Shockley-Hall-Read recombination rates of holes and electrons, μ_r are the hole and electron mobility, and D_r are the diffusion constants associated with holes and electrons. The space-dependent parameters γ_r are the quantum-correction factors associated with holes and electrons having the initial values of unity at the first iteration [21]. The parameter $N(z)$ is the space-dependent doping profile of the p^+-n-i_{MQB}-n^+ structured device [21]. The space-dependent electric potential ($V(z)$), electron ($n(z)$) density, hole ($p(z)$) density, electron current density ($J_n^{(total)}(z)$) and hole ($J_p^{(total)}(z)$) current density solutions for given biasing and optical illumination conditions at each iteration can be obtained by simultaneously solving the CLDD equations (1) – (3) by using finite difference method (FDM) subject to the following boundary conditions imposed at the depletion layer edges, i.e. at the p^+-n junction ($z = 0$) and at i_{MQB}-n^+ interface ($z = h_n + h_i$):

Electric Field Boundary Conditions:

$$V(z=0) = 0 \text{ and } V(z = h_n + h_i) = V_R, \tag{4}$$

Current Density Boundary Conditions:

$$NJ(z=0) = \left\{1 - \frac{2J_n^{(total)}(z=0)}{J_p^{(total)}(z=0) + J_n^{(total)}(z=0)}\right\}, \tag{5}$$

$$NJ(z = h_n + h_i) = \left\{\frac{2J_p^{(total)}(z = h_n + h_i)}{J_p^{(total)}(z = h_n + h_i) + J_n^{(total)}(z = h_n + h_i)} - 1\right\}, \tag{6}$$

where the normalized current density is given by $NJ = \left(J_p^{(total)} - J_n^{(total)}\right) \Big/ \left(J_p^{(total)} + J_n^{(total)}\right)$.

In group-III nitride semiconductor materials like wurtzite GaN and its binary compound $Al_xGa_{1-x}N$ are characterized by polarization properties. These materials are inherently characterized by spontaneous polarization properties under unstrained condition, which constitutes strain-independent built-in electrostatic fields [22]. The spontaneous polarization induced electric fields significantly influence the transport and optical properties of the group-III nitride-based nanostructures. On the other hand, both the wurtzite GaN and its binary compound $Al_xGa_{1-x}N$ are forced to exhibit piezoelectric polarization fields under strained condition [22]. In $Al_xGa_{1-x}N$/GaN/$Al_xGa_{1-x}N$ MQB structure, the lattice constants of GaN and $Al_xGa_{1-x}N$ are significantly different. Thus, in presence of pseudomorphic growth, both the active (GaN) and cladding ($Al_xGa_{1-x}N$) layers will be strained and constitute piezoelectric polarization fields [22]. The direction of spontaneous polarization is same as the growth direction, i.e. along the (0001) axis. However, the piezoelectric polarization may take any direction. In wurtzite nitrides, the growth direction is always kept along polar (0001) axis; consequently, a piezoelectric polarization is induced along the growth axis due to the existence of non-accommodated in-plane mismatches [23]. The sign of the piezoelectric polarization depends on the type of the epitaxial strain, i.e. either tensile or compressive. The polarization-induced electric field in the well (GaN) and barrier ($Al_xGa_{1-x}N$) layers of $Al_xGa_{1-x}N$/GaN/$Al_xGa_{1-x}N$ MQB structure are given by

$$\vec{\xi}_w^{(\chi)} = \frac{4\pi h_b\left(\vec{P}_b^{(\chi)} - \vec{P}_w^{(\chi)}\right)}{(h_b\epsilon_w + h_w\epsilon_b)}, \tag{7}$$

$$\vec{\xi}_b^{(\chi)} = \frac{4\pi h_w\left(\vec{P}_w^{(\chi)} - \vec{P}_b^{(\chi)}\right)}{(h_b\epsilon_w + h_w\epsilon_b)}, \tag{8}$$

where $\epsilon_{w,b}$ are the dielectric constants, and $h_{w,b}$ are the thicknesses of the well and barrier layers, $\chi \in \{sp, pz\}$ are the polarization type, i.e. spontaneous (sp) and piezoelectric

(pz) polarizations, and $\vec{P}_{w,b}^{(\chi)}$ are the χ-type polarization in GaN-well and $Al_xGa_{1-x}N$-barrier. It is noteworthy from the equations (7) and (8) that if $h_w = h_b$, then $\vec{\xi}_w^{(\chi)} = -\vec{\xi}_b^{(\chi)}$, which is relevant with the MQB structure under consideration ($h_w = h_b = 5$ nm). Therefore, in general, for an arbitrary strained condition, the total polarization-induced electric field is given by

$$\vec{\xi}_p = \sum\nolimits_{\chi\in\{sp,pz\}} \vec{\xi}_{b,w}^{(\chi)}. \tag{9}$$

In case of the pseudomorphically grown $Al_xGa_{1-x}N/GaN/Al_xGa_{1-x}N$ MQB structure on GaN substrate, in which $h_w = h_b$, the following relation will be maintained

$$\sum\nolimits_{\chi\in\{sp,pz\}} \vec{\xi}_w^{(\chi)} = -\sum\nolimits_{\chi\in\{sp,pz\}} \vec{\xi}_b^{(\chi)}. \tag{10}$$

Thus, the position-dependent total transverse polarization (P_t) in equation (1) can be determined from the relation $\vec{P}_t = \epsilon\vec{\xi}_p$, where ϵ position-dependent dielectric constant. The spontaneous and piezoelectric polarization components in $Al_xGa_{1-x}N$ cladding layers can be obtained from [23]

$$P_b^{(sp)} = xP_{AlN}^{(sp)} + (1-x)\,P_{GaN}^{(sp)}, \tag{11}$$

$$P_b^{(pz)} = 2S_{xy}\left\{e_{31} - \left(\frac{C_{13}}{C_{33}}\right)e_{33}\right\}, \tag{12}$$

where x is the Al mole fraction in $Al_xGa_{1-x}N$, $S_{xy} = \left(a_{GaN} - a_{Al_xGa_{1-x}N}\right)/a_{Al_xGa_{1-x}N}$ is the strain of x-$y$plane, e_{31}, e_{33} are the piezoelectric constants, C_{13}, C_{33} are the elastic constants, a_{GaN} and $a_{Al_xGa_{1-x}N}$ are the lattice constants of GaN and $Al_xGa_{1-x}N$ respectively. The model of Fiorentini et al. [22] has been taken into account in the present simulation method with 40% of the polarization charges compensated by defects and interface charges. Other material parameters related to the polarization in wurtzite group-III nitrides (GaN and $Al_xGa_{1-x}N$) are taken from the [23].

After obtaining the solutions of CLDD equations under a particular iteration, 1-D time-independent Schrödinger equations associated with conduction and valance bands are solved in order to take into account the bound-states in the quantum wells. The Schrödinger equations corresponding to the valance and conduction bands are given by

$$-\frac{d}{dz}\hat{z}.\left(\frac{\hbar}{2m_r^*}\frac{d\psi_r^{Z_r}}{dz}\hat{z}\right) + E_{V,C}\psi_r^{Z_r} = E_r^{Z_r}\psi_r^{Z_r}, \tag{13}$$

where $\hbar = h/2\pi$ is the normalized Planck's constant ($h = 6.62 \times 10^{-31}$ J s), m_r^* are the space-dependent effective mass of holes in valance band and electrons in conduction band, $\psi_r^{Z_r}$ and $E_r^{Z_r}$ are the wave-function and eigen-energy state solutions associated with the valance and conduction bands respectively, Z_r are the number of modes (typically $Z_r = 5 - 10$). The lowest energy state of the conduction band and highest energy state of the valance band in MQB structure can be obtained from

$$E_C = -qV + \frac{1}{2}\left\{E_g + k_BTln\left(\frac{N_C}{N_V}\right)\right\}, \tag{14}$$

$$E_V = E_C - E_g, \tag{15}$$

where T represents the temperature in Kelvin (K), $k_B = 1.38 \times 10^{-23}$ J K^{-1} is the Boltzmann constant, $V$is the space-dependent electric potential obtained as one of the solutions of CLDD equations, E_g is the space-dependent bandgap and $N_{C,V}$ are the effective density-of-states in conduction and valance bands respectively. Now, the quantum hole and electron densities can be calculated from'

$$r^{(qunt)} = \sum\nolimits_{Z_r}\left(N_r^{Z_r}\left|\psi_r^{Z_r}\right|^2\right), \tag{16}$$

where $N_r^{Z_r}$ are the sub-band hole and electron densities in valance and conduction bands of the MQBs respectively. These are determined from the knowledge of the 2-D density-of-states functions and Fermi-Dirac distribution functions associated with the hole and electron densities in valance and conduction bands of the MQBs respectively [21]. Finally, the space-dependent quantum-correction factors corresponding to the hole and electron densities are determined from

$$\left.\begin{array}{ll}\gamma_r & = \left\{\frac{r^{(qunt)}}{r}\right\} \quad \text{in } \Omega_{MQB} \\ & = 1 \qquad\qquad \text{Otherwise}\end{array}\right\}. \tag{17}$$

Through the space-dependent parameter γ_r, the quantum-corrections are introduced in the hole (p) and electron (n) densities of the CLDD equations (1) – (3) from the next iteration (iteration number ≥ 2). At the end of each iteration, the inter-iteration deviation of V, n, p, $J_n^{(total)}(z)$ and $J_p^{(total)}(z)$ are individually calculated [21]. The self-consistent solutions are assumed to be achieved, when all the inter-iteration deviations are found to be less than the order of 10^{-3} [21]. The self-consistent current density for given reverse bias and optical illumination condition can be determined from

$$J_{(SC)}^{(total)} = \frac{1}{H}\int_{z=-h_{p^+}}^{z=h_n+h_i+h_{n^+}}\left\{J_{n(SC)}^{(total)} + J_{p(SC)}^{(total)}\right\}dz, \tag{18}$$

where $H = h_{p^+} + h_n + h_i + h_{n^+}$ is the effective thickness of the device.

The multiplied responsivity of the MQB APD for a given reverse bias voltage V_R and for incident optical power P_{opt} of wavelength λ is given by

$$R(\lambda) = \left(\frac{A_j}{P_{opt}}\right)\left\{J_{(SC)}^{(total)}(\lambda) - J_{(SC)}^{(total)}(\lambda)\Big|_{P_{opt}=0}\right\}, \tag{19}$$

where $A_j = L_aW_a$ is the cross-sectional area of the p^+-n junction [21]. The term $J_{(SC)}^{(total)}(\lambda)$ is the self-consistent solution of the total terminal current (photocurrent plus dark current) for the bias voltage of V_R and incident optical power of P_{opt} of wavelength λ. The details of the algorithm for solving the SCQDD equations subject to appropriate boundary conditions and the method of calculating the self-consistent solution of total terminal current $J_{(SC)}^{(total)}(\lambda)$ for a given set of V_R, P_{opt} and λ is already reported elsewhere [19], [21]. The self-consistent dark current associated with the device for the

reverse bias voltage of V_R can be obtained from (for incident optical power $P_{opt} = 0$)

$$I_{(SC)}^{(dark)} = A_j J_{(SC)}^{(total)}(\lambda)\Big|_{P_{opt}=0}, \tag{20}$$

and therefore, the total photo current for the same amount of reverse bias voltage (V_R) and for the incident optical power of P_{opt} of wavelength λ is given by

$$I_{(SC)}^{(opt)}(\lambda) = \left\{A_j J_{(SC)}^{(total)}(\lambda) - I_{(SC)}^{(dark)}\right\}. \tag{21}$$

In the proposed MQB APD structure the light energy is illuminated on the p^+-GaN surface through an optical window of area $A_{ow} = L_{ow}W_{ow}$. Here, only the photo-generated electrons in the p^+-GaN layer injected to the n-GaN avalanche multiplication region and finally drifted through the multiple quantum wells before reaching the positively biased cathode. Since the charge multiplications only occur in n-GaN and MQB regions, electron current gets enough avalanche multiplication gain. On the other hand, photo-generated holes in the p^+-GaN region immediately reach the negatively biased anode and do not get opportunity to be multiplied. Therefore, the photo current in the proposed MQB APD is clearly electron dominated. The random nature of the electron multiplication process causes significant number of unwanted fluctuations in the total photo current; these unwanted fluctuations are known as avalanche noise. The noise performance of an APD is quantified by a parameter named excess noise factor (ENF). The ENF of the proposed MQB APD based on GaN/$Al_{0.3}Ga_{0.7}N$ hetero-structures can be expressed as [24]

$$F = 1 + \left\{\frac{\left(1 - \frac{1}{\langle M\rangle}\right)(1 - K_t)}{2 + P(1 + K_t)}\right\} \times \left\{2\left(\frac{1 - K_t P^2}{1 + K_t P}\right)\left[\langle M\rangle K_t\left(\frac{1+P}{1-K_t}\right) + \left(\frac{1}{1+P}\right)\right] - P\right\}, \tag{22}$$

where $\langle M\rangle$ is the multiplication gain associated with the electron-initiated multiplication process and the expression of $\langle M\rangle$ is given by

$$\langle M\rangle = \left\{\frac{(1+P)^m (1 - K_t)}{(1 + K_t P)^{m+1} - K_t (1 + P)^{m+1}}\right\}, \tag{23}$$

where m is the number of QB plus QW stages. The electron and hole ionization probabilities (P and Q respectively) per stage are given by

$$P, Q = \left\{exp\left(\int_{z=0}^{z=h_b+h_w} \varsigma_{n,p}^{(MQB)}(z)\, dz\right) - 1\right\}, \tag{24}$$

where $\varsigma_{n,p}^{(MQB)}$ are respectively the ionization rate of electrons and holes in MQB structure. The ratio $\varsigma_n^{(MQB)}/\varsigma_p^{(MQB)}$ can be calculated as function of electric field (ξ) by using the method prescribed by Chin et al. [25]. The ratio of electron ionization probability and hole ionization probability per stage of the MQWs denoted by K_t in equations (4) and (5) is given by

$$K_t = \left(\frac{Q}{P}\right). \tag{25}$$

After obtaining the spectral response and noise performance of the proposed MQB APD structure, finally the time and frequency response of that structure must be investigated. In order to obtain the time response a unit rectangular pulse having form

$$p_{rect}(t) = u(t) - u\left(t - \Delta_{pl}\right), \tag{26}$$

where Δ_{pl} is the duration of the pulse and $u(t)$ is the Heaviside step function (i.e, u(t) = 1 for $t \geq 0$ and $u(t) = 0$ for $t < 0$), is assumed to incident on the p^+-GaN surface through the optical window of area $A_{ow} = L_{ow}W_{ow}$. The unmultiplied time varying photo-generated electron and hole currents having both drift and diffusion components are calculated by considering the time dependent incident photon flux density of wavelength λ

$$\Phi_{(opt)}^{(\lambda)}(t) = \Phi_0^{(\lambda)} p_{rect}(t), \tag{27}$$

where $\Phi_0^{(\lambda)}$ is the amplitude of the incident optical flux density pulse, i.e.

$$\Phi_0^{(\lambda)} = \left\{\frac{P_{opt}\left(1 - R(\lambda)\right)\lambda}{A_{ow} hc}\right\}, \tag{28}$$

where $c = 3.0 \times 10^8$ m s^{-1} is the velocity of light in vacuum, $R(\lambda)$ is the reflectance of GaN surface [26], which is given by

$$R(\lambda) = \left\{\frac{n^{(GaN)}(\lambda) - n^{(air)}(\lambda)}{n^{(GaN)}(\lambda) + n^{(air)}(\lambda)}\right\}^2, \tag{29}$$

where $n^{(GaN)}(\lambda)$ and $n^{(air)}(\lambda)$ are the refractive indexes of GaN surface [26] and air at the wavelength of λ. Finally, the time-varying drift-diffusion equations such as Poisson's equation, carrier continuity equations and current density equations are simultaneously solved subject to appropriate time-varying boundary conditions at the depletion layer edges, in order to obtain the time and space dependent multiplied electron and hole photocurrents ($J_n^{(\lambda)}(x,t)$) and $J_p^{(\lambda)}(x,t)$). From knowledge of the device dimensions as well as electron and hole photocurrent solutions, the current response associated with the incident optical pulse can be determined. It is given by [27]

$$I^{(\lambda)}(t) = \left(\frac{A_j}{H}\right)\int_{x=-h_{p+}}^{x=h_n+h_i+h_{n^+}} \left\{J_n^{(\lambda)}(x,t) + J_p^{(\lambda)}(x,t)\right\} dx. \tag{30}$$

Fourier transform of $I^{(\lambda)}(t)$ provides the frequency domain current response of the device, which is given by

$$I^{(\lambda)}(f) = \int_{t=-\infty}^{t=+\infty} I^{(\lambda)}(t)\, exp(-j2\pi ft)\, dt. \tag{31}$$

Appropriate fast-Fourier transform (FFT) algorithm with sampling frequency $f_s > 10/\Delta_{pl}$ must be used to obtain $I^{(\lambda)}(f)$.

IV. CURRENT-VOLTAGE CHARACTERISTICS AND SPECTRAL RESPONSE

The proposed simulation methodology based on SCQDD model has been initially verified by comparing the simulation results of an AlGaN/GaN multi-quantum well (MQW) APD with the experimentally measured data of Zheng et al. [28]. Here, the simulations have been carried out on the MQW APD structure fabricated and tested by Zheng et al. [28] in the year 2016, under the dark and same optical illumination conditions, i.e. for $P_{opt} = 0$ and for incident optical power of $P_{opt} = 250$ pW from an UV light source of 350 nm wavelength respectively. Figure 3 (a) shows the current-voltage (I-V) characteristics of the MQW APD obtained from both simulation (present work) and experimental measurements (reported in [28]). The Figures 3 (b) and (c) show the simulated variations of the dark current (I_d) and photo-current (I_{ph}) with the applied reverse bias (V_R) ranging from 0 to 40 V and from 40 to 80 V respectively; those figures also illustrate the amount of deviation in the simulated values of I_d and I_{ph} with respect to the corresponding experimentally measured values at each data point. It can be observed from Figures 3 (a) – (c) that the simulation results are very close in agreement with the experimental data of Zheng et al. [28] and therefore, it validates the proposed simulation model for the further simulation study of the proposed $Al_{0.3}Ga_{0.7}N/GaN/Al_{0.3}Ga_{0.7}N$ MQB APD structure. The I-V characteristics of the $Al_{0.3}Ga_{0.7}N/GaN/Al_{0.3}Ga_{0.7}N$ MQB APD have now been obtained from the numerical simulations. The IV characteristics of the APD have been obtained under dark condition ($P_{opt} = 0$) and for different incident optical power ($P_{opt} = 10, 100, 500$ and 1000 mW) of wavelengths ranging from 100 – 2500 nm. Breakdown of the device occurs at around 10.3 – 10.4V at different illumination conditions. The dark current of the $GaN/Al_{0.3}Ga_{0.7}N$ MQB APD is found to be around 1.4×10^{-13} A at the reverse bias of 10.1V ($V_R <$ breakdown voltage (V_B)), which is significantly smaller than the simulated dark current of Si/3C-SiC MQB APD (0.24 – 0.40 nA at 9.0V of reverse bias) [29]. Breakdown characteristics of $GaN/Al_{0.3}Ga_{0.7}N$ MQB APD are considerably sharper than those of Si/3C-SiC MQB APDs. The I-V characteristics of $GaN/Al_{0.3}Ga_{0.7}N$ MQB APD under dark condition and for incident optical power of 10, 100, 500 and 1000 mW of wavelength 3.0 μm have been shown in Figure 4. For reverse bias of 10.2V just below the breakdown voltage, the photocurrent through the device is observed to be increased from 1.1pA to 0.29nA for the increment of the incident optical power from 10 mW to 1.0 W at $\lambda = 3.0$ μm.

The spectral response of an APD majorly depends on these factors such as (i) thickness of the absorption region (n-layer and total MQB layers) (ii) anti-reflection coating on the incidence surface (i.e. p^+-GaN surface) of the photon-flux and (iii) thickness of the anode contact layer (p^+-GaN layer). Moreover, the absorption coefficient of the base material system ($GaN/Al_{0.3}Ga_{0.7}N$) and structure of the absorption layer (MQB structure) are the key factors which determine the nature of the spectral response of the device. The spectral response of the $GaN/Al_{0.3}Ga_{0.7}N$ MQB APD at 10.2V reverse bias and 1 W of incident optical power of wavelengths ranging from 100nm – 6.5 μm has been shown in Figure 5. The spectral response of the APDS within the wavelength

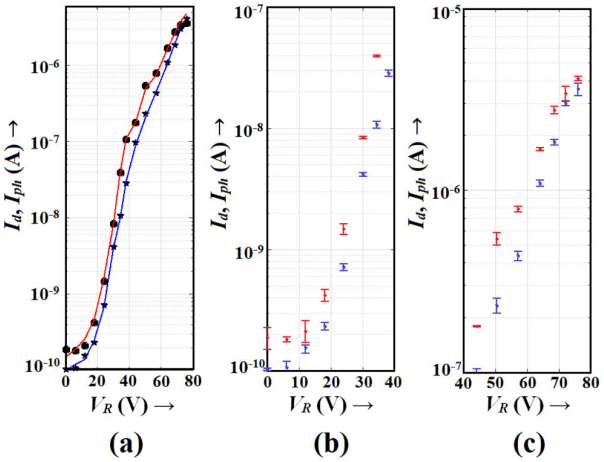

FIGURE 3. I-V characteristics of AlGaN/GaN MQW APD under the dark and optical illumination of 350 nm UV light with incident optical power of 250 pW; I-V curves: (a) experimental measured data of Zheng et al. [28] (solid black star markers (⋆) represent I_d, solid black circular markers (•) represent I_{ph}), and simulated data using the proposed model (solid blue line (–) represents I_d, and solid red line (–) represents I_{ph}); deviation of simulated data with the experimental data between the reverse bias voltage ranging from (b) 0 to 40 V and (c) 40 to 80 V (blue error bars represent ΔI_d, and red error bars represent ΔI_{ph}).

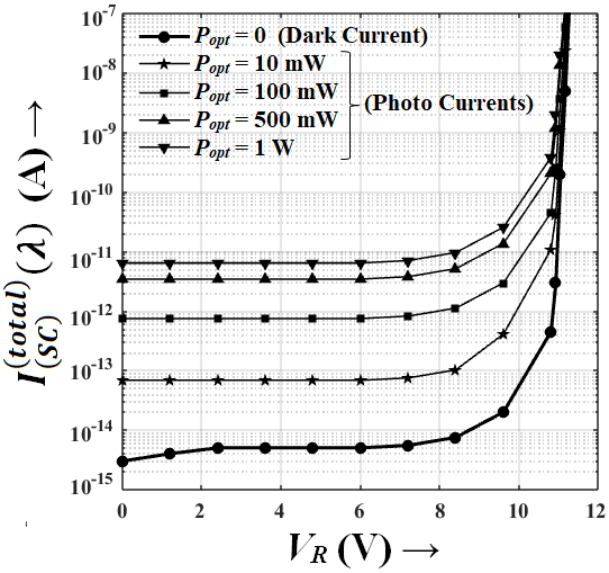

FIGURE 4. The I-V characteristics of the $GaN/Al_{0.3}Ga_{0.7}N$ MQB APD under dark condition and for different incident optical powers of wavelength 3.0 μm.

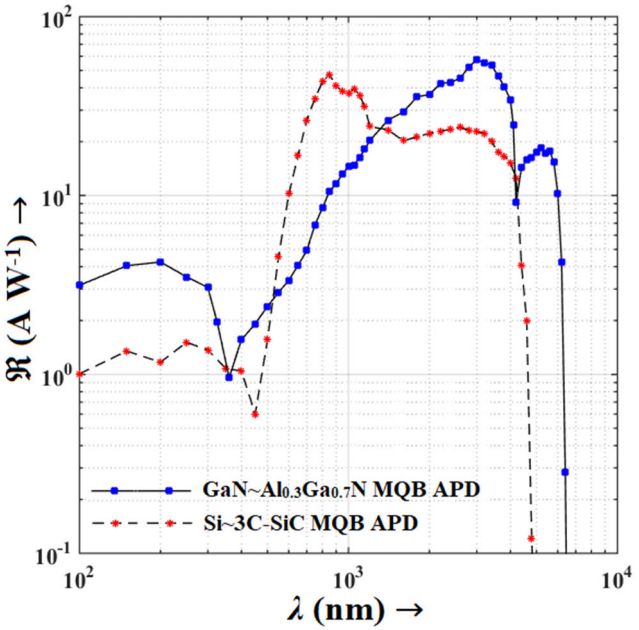

FIGURE 5. Variations of spectral responsivity of MQB APDs based on GaN/$Al_{0.3}Ga_{0.7}$N (reverse bias voltage of 10.2 V, and incident optical power of 1 W) and Si/3C-SiC (reverse bias voltage of 9.0 V, and incident optical power of 1 W) heterojunctions with wavelength.

range 100 – 360 nm (UV spectrum) is achieved due to the photon absorption in p^+- and n-GaN layers. Within this UV range the peak responsivity is 4.1 AW^{-1} is attained at 200 nm wavelength. Direct transitions of electrons from the energy states of valance band to the energy states of conduction band is the primary mechanism of photocurrent generation within this UV wavelength range. The inter sub-band transitions of electrons within the quantum wells of the MQB structure leads to the significant rise in responsivity of the APD within the visible spectrum (400 – 770 nm), near-infrared (700 – 1400 nm), shortwave-infrared (1400 – 3000nm), mid-infrared (3.0 – 6.0 μm) spectrums. The peak responsivity of 60 AW^{-1} is achieved at 3.0 μm wavelength.

The carbon dioxide (CO_2) absorption causes a dip in the responsivity at the wavelength of 4.3 μm. the effect of the CO_2 absorption has been included in the simulation through the experimental data of absorption coefficients at room temperature. The spectral response of Si/3C-SiC MQB APD at reverse bias of 9.0 V and for incident optical power of 1 W of wavelength range 100 – 4000 nm is also shown in Figure 5. Unlike the GaN/$Al_{0.3}Ga_{0.7}$N MQB APD the transition of band-to-band absorption in barrier material (wider bandgap) to quantum well inter sub-band absorption occurs at 450 nm; the peak responsivity of 1.6 AW^{-1} can be achieved at 260 nm in Si/3C-SiC MQB APD with the detectable UV spectrum of it. The peak responsivity Si/3C-SiC MQB APD occurs at 350 nm which is around 50 AW^{-1} and its responsivity gradually decays to 15 AW^{-1} at 4.0 μm wavelength after which sharp decay in the responsivity versus wavelength curve is observed. Therefore, GaN/$Al_{0.3}Ga_{0.7}$N MQB APD capable of detecting wavelengths up to 6.0 μm, whereas the maximum detectable wavelength of Si/3C-SiC MQB APD is around 4.0 μm.

V. EXCESS NOISE CHARACTERISTICS

The valance band offset (VBO) in GaN/$Al_{0.3}Ga_{0.7}$N heterojunctions is $\Delta E_v = 0.3x$ eV, whereas conduction band offset (CBO) of those is $\Delta E_c = E_g(x) - \Delta E_v - E_g$; where $E_g(x) = 6.13x + 3.42(1\text{-}x) - 1.0(1\text{-}x)x$ eV is the bandgap of $Al_xGa_{1\text{-}x}N$ at room temperature and $E_g = 3.42$ eV is the bandgap of GaN at room temperature (300K) [30]. Therefore, the values of VBO and CBO in the type-I band alignment of $Al_{0.3}Ga_{0.7}N$ are $\Delta E_v = 0.09$ eV and $\Delta E_c = 0.513$ eV respectively. Thus, in GaN/$Al_{0.3}Ga_{0.7}$N heterojunction, the discontinuity in conduction band ($\Delta E_c = 0.513$eV) is significantly larger as compared to the discontinuity in valance band ($\Delta E_v = 0.09$ eV). The ionization rate of holes is larger than of electrons in GaN, while ionization rate of electrons is larger than holes in AlN [31], [32], [33]. Although the ratio of ionization rate of holes to ionization rate of electrons (ς_p/ς_n) is greater than one in bulk GaN, due to the greater conduction band discontinuity in GaN/$Al_{0.3}Ga_{0.7}$N heterojunctions the ratio (ς_p/ς_n) reduces slightly in GaN/$Al_{0.3}Ga_{0.7}$N MQB structures [30]. As a result of that elimination of secondary carrier multiplication cannot be achieved like Si/3C-SiC structures, in which $\Delta E_v > \Delta E_c$. Therefore, in order to reduce the excess noise in GaN/$Al_{0.3}Ga_{0.7}$N MQB APD an extra n-GaN dedicated layer has been introduced to restrict the electron dominated carrier multiplication within a narrow region (nearly around 20 nm thick). By providing the spectral restrictions to the avalanche multiplication phenomenon, better excess noise characteristics can be achieved in GaN/$Al_{0.3}Ga_{0.7}$N MQB APD, having p^+-n-i_{MQB}-n^+ structure as compared to the Si/3C-SiC having p^+-i_{MQB}-n^+ structure. The gain ($\langle M \rangle$) versus bias voltage (V_R) curve of MQB APD based on GaN/$Al_{0.3}Ga_{0.7}$N heterojunctions is shown in Figure 6 (a). The Figure 6 (a) also shows the $\langle M \rangle$ versus V_R characteristics of Si/3C-SiC MQB APDs with different number of quantum barriers (N_b), such as $N_b = 1$ in APD1, $N_b = 3$ in APD2, and $N_b = 5$ in APD3 [24]. It is observed from Figure 6 (a) that at the bias voltage of 9.0 V, the gain of Si/3C-SiC MQB APDs vary from 102.29 to 118.65; whereas the peak gain of 92.69 is achieved in GaN/$Al_{0.3}Ga_{0.7}$N MQB APD at the bias voltage of 10.2 V. The variation of excess noise factor (ENF) of GaN/$Al_{0.3}Ga_{0.7}$N MQB APD with multiplication gain ($\langle M \rangle$) has been shown in Figure 6 (b). It is noteworthy from Figure 6 (b) that the ENF of GaN/$Al_{0.3}Ga_{0.7}$N MQB APD varies from 1.62 to 5.95 for the multiplication gain range of 1 – 100, while the lowest achievable ENF in Si/3C-SiC MQB APD is ranging from 1.58 – 10.9 for the same multiplication gain range. Therefore, clearly the GaN/$Al_{0.3}Ga_{0.7}$N MQB APD is less noisy as compared to its Si/3C-SiC counterpart.

VI. SIGNAL-TO NOISE RATIO AND OPTIMUM GAIN

The avalanche multiplication process typically begins when a thermally generated electron is present within the avalanche

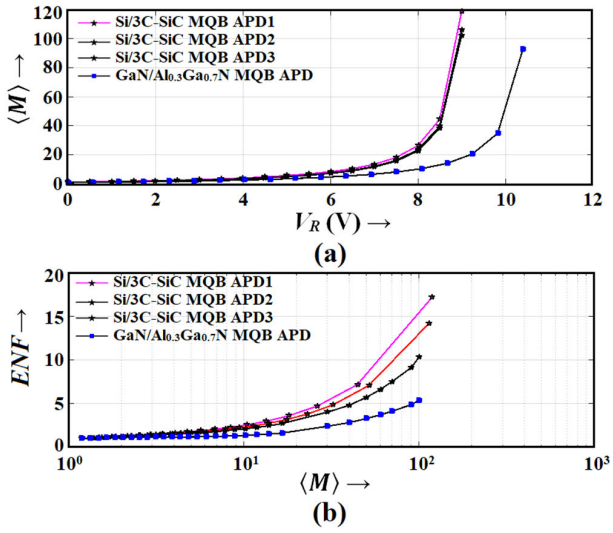

FIGURE 6. Variations of (a) gain with reverse bias voltage, and (b) excess noise factor with gain in MQB APDs based on GaN/$Al_{0.3}Ga_{0.7}N$ and Si/3C-SiC [24] heterojunctions.

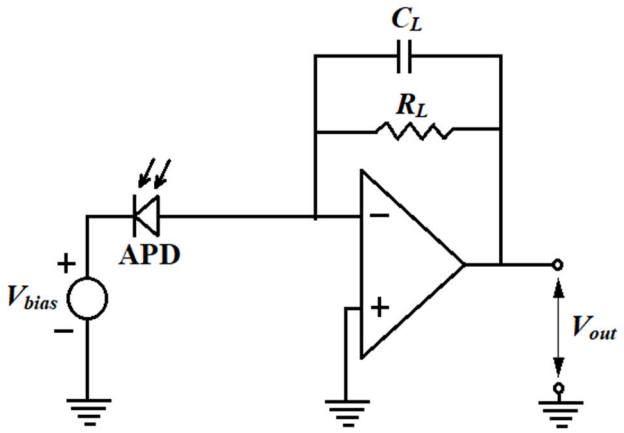

FIGURE 7. Schematic of the read-out circuit.

zone, and when combined with other non-optical sources of noise, it results in a multiplied dark current as follows:

$$I_{(SC)}^{(Mult\_dark)} = I_{(SC)}^{(dark)} \langle M \rangle. \tag{32}$$

The multiplied dark current adds excess noise, and the shot noise component of this multiplied dark current is expressed as:

$$\left\langle I_{(SC)}^{(Mult_{dark})} \right\rangle = \left\{ 2qI_{(SC)}^{(dark)} \langle M \rangle^2 F \right\}^{\frac{1}{2}}. \tag{33}$$

Considering both the multiplied dark and photo currents, the expression of total output current (signal) and output voltage are expressed as:

$$I_L = \left(I_{(SC)}^{(opt)} + I_{(SC)}^{(dark)} \right) \langle M \rangle \quad \text{and} \quad V_L = I_L R_L. \tag{34}$$

The shot-noise component due to the total output current (signal) can be expressed as:

$$\langle I_L \rangle = \left\{ 2q \left(I_{(SC)}^{(opt)} + I_{(SC)}^{(dark)} \right) \langle M \rangle^2 F \right\}^{\frac{1}{2}}. \tag{35}$$

To characterize the noise characteristics of an APD, we illustrate a standard read-out circuit for an APD in Figure 7 [34]. This circuit comprises of a steady voltage source for providing reverse bias (V_{bias}) to the APD and a trans-impedance amplifier, as depicted in Figure 7. The trans-impedance amplifier serves to convert and amplify the overall output current from the APD into a corresponding output voltage V_{out}. Under a first-order approximation, the output voltage resulting from the signal power is given by

$$V_{out} = I_L R_L. \tag{36}$$

Additional standard assumptions regarding the amplifier include a 3-dB bandwidth (B_n) that aligns with the rise time of the photocurrent pulse, a linear response, and the absence of stray capacitances. Moreover, the amplifier's noise contribution is characterized by the inclusion of a noise current spectral density $\langle I_n \rangle$ at its output. The corresponding amplified voltage, V_n, obtained by multiplying it by the square-root of the bandwidth (B_n), is expressed as:

$$V_n = \langle V_n \rangle (B_n)^{\frac{1}{2}} = \langle I_n \rangle R_L (B_n)^{\frac{1}{2}}. \tag{37}$$

The resistor R_L determines the gain of the trans-impedance amplifier and introduces a Johnson noise current of

$$\langle I_{Th} \rangle = \frac{4k_B T}{R_L}. \tag{38}$$

The capacitor C_L serves as phase compensation, reducing gain peaking in the read-out circuit at higher frequencies [35]. Taking into account the 3-dB bandwidth B_n (i.e., the amplifier's noise bandwidth), the expression for the Johnson noise voltage is as follows:

$$\langle V_{Th} \rangle = (4k_B T B_n R_L)^{\frac{1}{2}}. \tag{39}$$

The shot noise voltage component due to the signal is given by

$$\langle V_L \rangle = \left\{ 2qB_n \left[\left(I_{(SC)}^{(opt)} + I_{(sc)}^{(dark)} \right) \langle M \rangle^2 F \right] \right\}^{\frac{1}{2}} R_L. \tag{40}$$

Summing up the previously mentioned noise currents in a quadrature manner and converting them into a voltage results in the overall noise voltage at the amplifier's output. This total noise voltage at the amplifier's output can be expressed as:

$$\begin{aligned} \langle V_{out} \rangle &= \left\{ \langle V_L \rangle^2 + \langle V_{Th} \rangle^2 + V_n^2 \right\}^{\frac{1}{2}} \\ &= \left\{ 2qB_n \left[\left(I_{(SC)}^{(opt)} + I_{(SC)}^{(dark)} \right) \langle M \rangle^2 F \right] R_L^2 \right. \\ &\quad \left. + B_n \left(4k_B T R_L + \langle V_n \rangle^2 \right) \right\}^{\frac{1}{2}}. \end{aligned} \tag{41}$$

The Signal-to-Noise Ratio (SNR) of the APD and the read-out circuit is defined as the ratio of the signal output voltage to the total noise voltage and is given by [34] and [35], (42), as shown at the bottom of the next page.

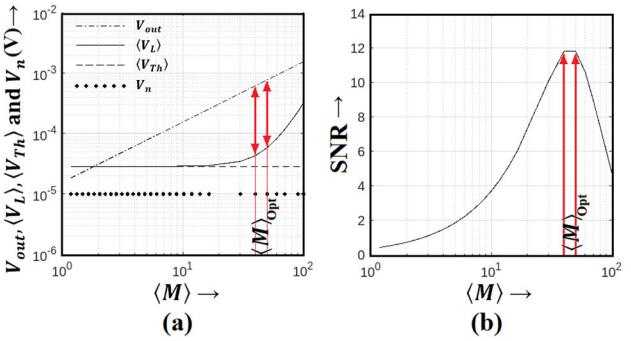

FIGURE 8. Noise characteristics of the MQB APD based on GaN/$Al_{0.3}Ga_{0.7}N$ heterojunctions.

A typical transimpedance amplifier with $B_n = 50$ MHz and amplification noise voltage spectra density $\langle V_n \rangle = 1.414 \times 10^{-7}$ V $Hz^{-1/2}$ terminated with a resistance of $R_L = 1.0$ KΩ at an effective input noise temperature $T = 300$ K [34] has been considered for the SNR calculation and determination of optimum optical gain of the MQB APD based on GaN/$Al_{0.3}Ga_{0.7}N$ heterojunctions. Figure 8 (a) illustrates the fluctuations in several key parameters: the output signal voltage (V_{out}), the shot noise voltage component ($\langle V_L \rangle$), the Johnson noise voltage ($\langle V_{Th} \rangle$), and the noise voltage at the amplified output (V_n), all in relation to the multiplication gain ($\langle M \rangle$) associated with the electron-initiated multiplication process. In contrast, Figure 8 (b) depicts the variation of the SNR as a function of $\langle M \rangle$. Notably, Figure 8 (b) reveals that the SNR reaches its peak within a multiplication gain range of 40 to 50. Consequently, this range of 40 to 50 can be considered as the optimal gain values ($\langle M \rangle_{opt}$), maximizing SNR at the output of the trans-impedance amplifier. It's worth noting that enhancing the trans-impedance amplifier circuit can further improve the output SNR, but it won't affect the range of the optimal gain.

VII. TIME AND FREQUENCY RESPONSES

The pulse responses of GaN/$Al_{0.3}Ga_{0.7}N$ and Si/3C-SiC MQB APDs are shown in Figure 9. The pulse width $\Delta_{pl} = 0.4$ ps and height $\Phi_0^{(\lambda)} = 70.15 \times 10^{30}$ $m^{-2}s^{-1}$ are kept fixed, but the wavelengths are selected separately for each APD. The wavelength of the incident optical pulse is selected for each APD for which their respective responsivity peaks are attained. Therefore, 3.0 and 0.8 μm wavelengths are selected for GaN/$Al_{0.3}Ga_{0.7}N$ and Si/3C-SiC MQB APDs respectively. The current responses of the APDs associated with the similar input optical pulse show that significantly narrower current response can be achieved in the proposed GaN/$Al_{0.3}Ga_{0.7}N$ MQB APD as compared to Si/3C-SiC MQB APD. Primarily the current response possesses multiple peaks (i) first or major peak is associated with the original injected electrons and (ii) subsequent minor peaks are associated with the secondary generation of the electron-hole pairs due to charge multiplication phenomenon at the active regions. Narrow down of the avalanche zone due to the introduction of n-type dedicated multiplication layer in GaN/$Al_{0.3}Ga_{0.7}N$ MQB APD the secondary electron-hole pair generation is supressed in MQB layers. As a result of that the minor peaks of the current response are significantly supressed in GaN/$Al_{0.3}Ga_{0.7}N$ MQB APD as compared to the Si/3C-SiC MQB APDs. Thus GaN/$Al_{0.3}Ga_{0.7}N$ MQB APDs have significantly shorter response time ($\tau_{rs} = 2.4$ ps) as compared to the Si/3C-SiC MQB APDs ($\tau_{rs} = 4.2$ ps). The normalised frequency responses of the APDs have been shown in Figure 10, which are obtained from the FFT of corresponding time responses shown in Figure 9. Shorter time response of GaN/$Al_{0.3}Ga_{0.7}N$ MQB APD leads to significantly broader 3-dB bandwidth (BW = 274.5 GHz) as compared to the Si/3C-SiC MQB APD (BW = 78.4GHz). Therefore, nearly around 3.5 times higher bandwidth is achievable in p^+-n-i_{MQB}-n^+ structured MQB APD based on GaN/$Al_{0.3}Ga_{0.7}N$ material system as compared to its p^+-i_{MQB}-n^+ structured Si/3C-SiC counterpart at their respective wavelengths corresponding to the responsivity peaks (i.e., 3.0 and 0.85 μm respectively).

VIII. PERFORMANCE LIMITATIONS

The MQB APD proposed here features a vertical illumination structure, where the photo-generated charge carriers are generated at the top layer (p^+-GaN) of the APD. Electrons and holes then travel along the same axis (z-axis) parallel to the axis of the incident light. This vertical illumination design comes with an inherent trade-off between carrier transit time and responsivity. The convenient optical coupling is a notable advantage of vertical illumination structure. Lateral illumination APD structures induce the optical signal perpendicular to the carrier's travel direction, allowing for a relaxation of the trade-off between carrier transport distance and optical path length. This, in turn, eases the trade-off between carrier transit time and responsivity. Nevertheless, a trade-off still exists between the resistance-capacitance (RC) time constant and optical path length in such lateral structures. The proposed device structure, as depicted in Figure 1, incorporates vertical illumination and a field-confinement configuration. It's worth noting that in the structure shown in Figure 1,

$$SNR = \frac{V_{out}}{\langle V_{out} \rangle} = \frac{I_L R_L}{\left\{2qB_n \left[\left(I_{(SC)}^{(opt)} + I_{(SC)}^{(dark)}\right)\langle M \rangle^2 F\right] R_L^2 + B_n \left(4k_B T R_L + \langle V_n \rangle^2\right)\right\}^{\frac{1}{2}}}. \quad (42)$$

TABLE 2. Comparison between the proposed APD with the earlier reported group-III nitride-based APDs.

Sl. No.	Spectrum	Electron/Hole Initiated	λ (nm)	Dark Current Density (A m^{-2})	$\Re$ (mA W^{-1})	$\lvert V_R \rvert$ (V)	ENF at $\langle M \rangle$ = 100	Type of the Study	Ref.
1	UV	Electron	350	1.05×10^{-6}	---	65.00	2.2	Experimental	[28]
		Hole	350	1.50×10^{-5}	60000	278.0	---	Experimental	[41]
		Hole	340	10.0×10^{-3}	150	66.5	---	Experimental	[42]
		Hole	255	0.80	---	80.0	---	Experimental	[43]
		Electron	365	4.00×10^{-5}	140	95.4	---	Experimental	[44]
2		Electron	350	9.33×10^{-5}	921	10.20	5.95	Simulation	Present Work
3	IR	Electron	1460	10.00×10^{-3}	58600	0.50	---	Experimental	[45]
4		Electron	1500	9.33×10^{-5}	30000	10.20	5.95	Simulation	Present Work

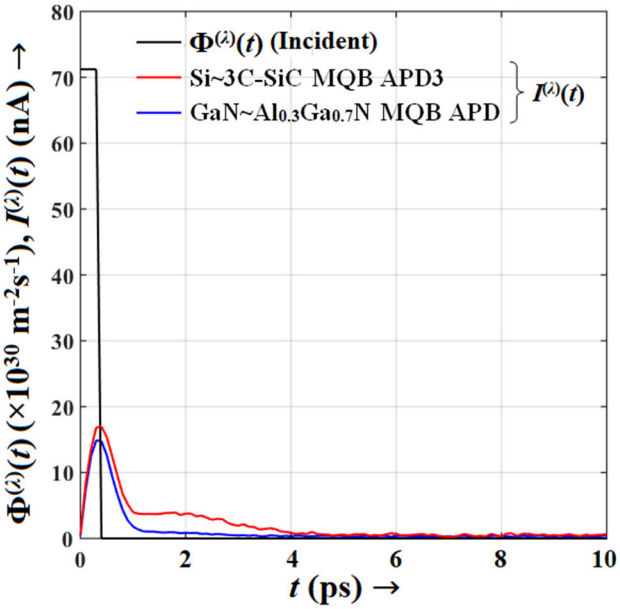

FIGURE 9. Pulse response currents of MQB APDs based on GaN/Al$_{0.3}$Ga$_{0.7}$N (bias voltage V_R = 10.2 V) and Si/3C-SiC (bias voltage V_R = 9.0 V) heterojunctions as function of time due to the incident rectangular pulse of photon flux density of 70.15 × 10^{30} m^{-2}s^{-1} and pulse width of 0.4 ps.

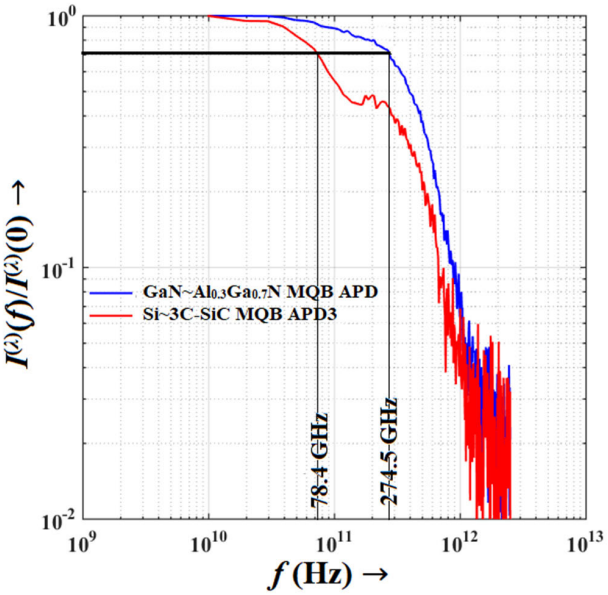

FIGURE 10. Frequency response of MQB APDs based on GaN/Al$_{0.3}$Ga$_{0.7}$N (bias voltage V_R = 10.2 V, wavelength 3.0 μm) and Si/3C-SiC (bias voltage V_R = 9.0 V,, wavelength 0.85 μm) heterojunctions; calculated for the incident rectangular pulse of photon flux density of 70.15 × 10^{30} m^{-2}s^{-1} and pulse width of 0.4 ps.

the total thickness of the MQB absorption layer (95 nm) and the doping density of this layer (10^{21} m^{-3}) determine the thickness of the depletion layer. Any deviation in this thickness will result in changes in responsivity, device capacitance, and operational speed. Therefore, for practical APDs employing this structure, precise control over the thickness of each quantum well (GaN), barrier (Al$_{0.3}$Ga$_{0.7}$N) layer, and their respective *n*-type doping concentrations is crucial.

In addition to the limitations mentioned earlier, there exists another factor in APDs that significantly impacts their performance in terms of responsivity, bandwidth, and noise characteristics. This factor is known as avalanche build-up time or avalanche response time, and it is closely tied to the properties of the avalanche layer, including its material composition and thickness. The processes of avalanche multiplication have an inherent finite response time; time required to attain the multiplication gain $\sim10^6$ is generally referred as avalanche response time [37], [38]. When the ionization coefficients of both electrons and holes are nearly identical and these carriers travel in opposite directions within the avalanche layer, creating new electrons and holes in the process. This behaviour introduces a delay in effectively sweeping out the ionized carriers from the avalanche layer. Since the avalanche multiplication and transport processes involve inherent randomness, this delay contributes to an increase in noise current. Consequently, a higher gain typically leads to a longer delay in carrier transit time and greater noise. To quantify this delay and noise impact, two

TABLE 3. Comparison between the proposed APD and other state-of-the-art near-IR to mid-IR photodetectors.

Sl. No.	λ (μm)	Mechanism	Material System*	$\Re$ (mA W^{-1})	$\lvert V_R \rvert$ (V)	BW (GHz)	Type of the Study	Ref.
1	0.85	Intersubband Transition	M~(Si~SiC~Si)$_{MQB}$~M	50000.00	9.0	78.40	Simulation	[21, 27]
2	**0.85**	**Intersubband Transition**	**M~(GaN~AlGaN~GaN)$_{MQB}$~M**	**10500.00**	**10.2**	**---**	**Simulation**	**Present Work**
3	1.16	Photovoltaic	M~MoTe$_2$~M	4.80	0	0.200	Experimental	[46]
4	1.31	Photovoltaic and Photoconductive	MoTe$_2$~G	400.00	3.0	0.500	Experimental	[47]
5	1.26 – 1.34	Photovoltaic and Photoconductive	MoTe$_2$~G	150.00	0.6	12.0 – 46.0	Experimental	[48]
6	1.35	Photovoltaic	M~G~M	200.00	0.5	---	Experimental	[49]
7	1.55	Photovoltaic	M~G~M	50.00	0	3.0 – 110.0	Experimental	[50-54]
8	1.55	Photo-thermoelectric	M~G~M	78.00	0	12.0 – 67.0	Experimental	[55-61]
9	1.55	Direct tunnelling and Fowler-Nordheim tunnelling	G~BN~G	240.00	10.0	28.00	Experimental	[62]
10	1.55	Internal photon emission	G~Si	130.00	1.5	---	Experimental	[63]
11	1.55	Internal photon emission	G~Si	11.00	0	> 50.0	Experimental	[64]
12	**1.55**	**Intersubband Transition**	**M~(GaN~AlGaN~GaN)$_{MQB}$~M**	**30000.00**	**10.2**	**---**	**Simulation**	**Present Work**
13	2.00	Bolometric	M~G~M	70.00	0.3	20.0	Experimental	[65]
14	2.00	Photovoltaic	M~BP~M	307.00	0.4	0.5 – 1.33	Experimental	[66]
15	2.75	Internal photon emission	G~Si	130.00	1.5	---	Experimental	[63]
16	**3.00**	**Intersubband Transition**	**M~(GaN~AlGaN~GaN)$_{MQB}$~M**	**60000.00**	**10.2**	**274.5**	**Simulation**	**Present Work**
17	3.00	Intersubband Transition	M~(Si~SiC~Si)$_{MQB}$~M	21500.00	9.0	78.40	**Simulation**	[21, 27]
18	3.68	Photo-gating	M~BP~M	23000.00	1.0	---		[67]
19	3.825	Photo-gating	M~BP~M	11310.00	0.5	5.5×10^{-7}	Experimental	[68]
20	**4.00**	**Intersubband Transition**	**M~(GaN~AlGaN~GaN)$_{MQB}$~M**	**33000.00**	**10.2**	**---**	**Simulation**	**Present Work**
21	4.00	Photo-gating	M~BP~M	2000.00	1.0	---	Experimental	[67]
22	**6.00**	**Intersubband Transition**	**M~(GaN~AlGaN~GaN)$_{MQB}$~M**	**16000.00**	**10.2**	**---**	**Simulation**	**Present Work**
23	4.30 – 10.00	Interlayer exciton	WS$_2$~HfS$_2$	3.51×10^{6}	1.5	2.0×10^{-7}	Experimental	[69]
24	3.40 – 12.00	Bolometric	M~G~M	5.10	0.5	0.047	Experimental	[70]

*M ≡ Metal, G ≡ Graphene, BP ≡ Black Phosphorus, MoTe$_2$ ≡ Molybdenum Ditelluride, WS$_2$ ≡Tungsten Disulfide and HfS$_2$ ≡ Hafnium Disulfide

essential metrics are considered: the gain-bandwidth product (GBP) and the avalanche response time (τ_A) [37]. These metrics vary for different materials, and they can even differ based on the type of injection carriers [37]. Hence, selecting the appropriate material for the avalanche layer is a critical decision. In this context, an n-GaN avalanche layer with a doping density of 2.0×10^{23} m^{-3} has been chosen. This n-type GaN layer exhibits an exceptionally low avalanche response time (approximately 10^{-16} seconds [37]) and a notably high GBP (around 300 GHz [39]). It is worth noting that thinning the avalanche layer, a phenomenon known as the ''dead-space effect'' [40], can further improve GBP and τ_A. However, it's essential to strike a balance between the material composition and thickness of the avalanche layer, while considering the trade-off between GBP, τ_A, and tunnelling dark current, as a thin avalanche layer can increase the latter [29].

IX. COMPARISON WITH EXISTING PHOTODETECTORS

In this section, initially the performance of the proposed GaN/$Al_{0.3}Ga_{0.7}$N/GaN MQB APD has been compared with some group-III nitride-based UV and IR detectors [28], [41], [42], [43], [44], [45]. The said performance comparison has been presented in Table 2. It can be observed from Table 2 that the performance of the proposed MQB structure is fairly comparable with the existing group-III nitride-based UV and IR detectors. However, the notable advantage of the proposed MQB APD is its wider detection spectrum (starting from UV spectrum, extended up to the mid-IR spectrum (up to 6.0 μm)) as compared to the other state-of-the-art detectors with considerable narrow detection spectrum [28], [41], [42], [43], [44], [45]. The performance of the proposed GaN/$Al_{0.3}Ga_{0.7}$N/GaN MQB APD has also been compared with various state-of-the-art near-IR and mid-IR photo-detectors available in literature [46], [47], [48], [49], [50], [51], [52], [53], [54], [55], [56], [57], [58], [59], [60], [61], [62], [63], [64], [65], [66], [67], [68], [69], [70]. The important performance parameters like responsivity, operating bias voltage and bandwidth are compared with other existing photodetectors within the wavelength range of 0.85 – 12.0 μm; the summary of the comparative study has been listed in Table 3. The primary mechanism behind the IR detection of the GaN/$Al_{0.3}Ga_{0.7}$N MQB APD is the inter sub-band transitions of electrons within the quantum wells. The earlier reported Si/3C-SiC MQB APD also utilises the same mechanism for IR detection. However other state-of-the-art IR detectors utilises several other mechanisms like photovoltaic, photoconductive, photo-thermo-elective, direct and Fowler-Nordheim tunnelling internal photon-emission, bolometric, photo-gating, interlayer excitons, etc [46], [47], [48], [49], [50], [51], [52], [53], [54], [55], [56], [57], [58], [59], [60], [61], [62], [63], [64], [65], [66], [67], [68], [69], [70]. Comparative study shows that the earlier reported Si/3C-SiC MQB APD proposes better responsivity at 0.85 μm wavelength, but its bandwidth is 3.5 times smaller than the proposed GaN/$Al_{0.3}Ga_{0.7}$N MQB APD. At 1.16 – 3.00 μm wavelength range the proposed APD shows the maximum responsivity and bandwidth among all existing IR detectors. However, the operating bias volage requirement of the proposed APD is nearly one order higher than the others. Waveguide integrated black phosphorous photodiodes fabricated and tested by Huang et al. [67] and Ma et al. [68] in years 2019 and 2020 respectively are the nearest competitors of the proposed APD in terms of responsivity within the wavelength range of 3.0 – 4.0 μm. However, the bandwidth of the proposed MQB APD is significantly higher than the black phosphorous photodetectors. Again, within the 4.0 – 6.0 μm wavelength range the optoelectronic performance of the proposed MQB APD is found to be significantly better as compared to the waveguide integrated black phosphorous photo-detectors, mid-IR photodetectors based on interlayer excitons in 2-D heterostructures and graphene mid-IR bolometer [69], [70].

X. CONCLUSION

A GaN/Al_xGa_{1-x}N/GaN MQB APD structure has been proposed and studied in this paper in order to investigate its potentiality to detect long wavelength IR signals up to 6.0 μm wavelength. A self-consistent quantum drift-diffusion (SCQDD) model developed by the authors has been used to determine the current-voltage characteristics under dark and illuminated conditions, spectral response, excess noise properties, time and frequency responses. Results show that the proposed MQB APD attains peak responsivity of 60 AW^{-1} at 3.0 μm wavelength. Incorporation of a dedicated thin n-GaN layer for avalanche multiplication in between the p^+-GaN contact layer and MQB constant field drift layer ensures significantly low noise equivalent power under normal operating conditions at room temperature (300 K). Optical pulse response of the device reveals that restricting the charge multiplication within a narrow avalanche zone near the p^+-n junction able to supress the minor peaks of the current response and consequently significantly narrow pulse response can be achieved. Narrow pulse response leads to broad bandwidth of 274.5 GHz, which is significantly broader than the existing IR photo-detectors. The performance of the proposed GaN/$Al_{0.3}Ga_{0.7}$N/GaN MQB APD has been compared with various state-of-the-art near IR mid IR photo detectors available in literature, and found to be highly promising for long wavelength IR detection up to 6.0 μm wavelength.

REFERENCES

[1] M. A. Othman, S. N. Taib, M. N. Husain, and Z. A. F. M. Napiah, ''Reviews on avalanche photodiode for optical communication technology,'' *ARPN J. Eng. Appl. Sci.*, vol. 9, no. 1, pp. 35–44, 2004.

[2] S. Masudy-Panah, M. K. Moravvej-Farshi, and M. Jalali, ''Temperature dependent characteristics of submicron GaAs avalanche photodiodes obtained by a nonlocal analysis,'' *Opt. Commun.*, vol. 282, no. 17, pp. 3630–3636, Sep. 2009.

[3] S. Masudy-Panah and M. K. Moravvej-Farshi, ''An analytic approach to study the effects of optical phonon scattering loss on the characteristics of avalanche photodiodes,'' *IEEE J. Quantum Electron.*, vol. 46, no. 4, pp. 533–540, Apr. 2010.

[4] S. Masudy-Panah, "Nonlocal analysis to study of the impact ionization and avalanche characteristics of deep submicron Si devices," *Solid State Commun.*, vol. 151, no. 8, pp. 610–614, Apr. 2011.

[5] S. Masudy-Panah and V. A. Tikkiwal, "Velocity enhancement in APDs with sub-100-nm multiplication region," *Opt. Commun.*, vol. 346, pp. 167–171, Jul. 2015.

[6] I. Wegrzecka, M. Grynglas, J. Bar, A. Uszynski, R. Grodecki, P. Grabiec, S. Krzeminski, and T. Budzynski, "Design and properties of silicon avalanche photodiodes," *Opto-Electron. Rev.*, vol. 12, no. 1, pp. 95–104, 2004.

[7] K. F. Brennan and J. Haralson, "Invited review: Superlattice and multiquantum well avalanche photodetectors: Physics, concepts and performance," *Superlattices Microstruct.*, vol. 28, no. 2, pp. 77–104, Aug. 2000.

[8] L. Yang, S. N. Dzhosyuk, J. M. Gabrielse, P. R. Huffman, C. E. H. Mattoni, S. E. Maxwell, D. N. McKinsey, and J. M. Doyle, "Performance of a large-area avalanche photodiode at low temperature for scintillation detection," *Nucl. Instrum. Methods Phys. Res. A, Accel. Spectrom. Detect. Assoc. Equip.*, vol. 508, no. 3, pp. 388–393, Aug. 2003.

[9] I. Britvitch, K. Deiters, Q. Ingram, A. Kuznetsov, Y. Musienko, D. Renker, S. Reucroft, T. Sakhelashvili, and J. Swain, "Avalanche photodiodes now and possible developments," *Nucl. Instrum. Methods Phys. Res. A, Accel. Spectrom. Detect. Assoc. Equip.*, vol. 535, nos. 1–2, pp. 523–527, Dec. 2004.

[10] D. Renker, "Properties of avalanche photodiodes for applications in high energy physics, astrophysics and medical imaging," *Nucl. Instrum. Methods Phys. Res. A, Accel. Spectrom. Detect. Assoc. Equip.*, vol. 486, nos. 1–2, pp. 164–169, Jun. 2002.

[11] J. Pansarat, "Avalanche photodiodes for particle detection," *Nucl. Instr. Meth.*, vol. 389, p. 186, Jan. 1997.

[12] H. Uemura, Y. Kurita, and H. Furuyama, "12.5 Gb/s optical driver and receiver ICs with double-threshold AGC for SATA out-of-band transmission," *IEEE J. Solid-State Circuits*, vol. 51, no. 7, pp. 1641–1650, Jul. 2016.

[13] J. Joo, K. S. Jang, and S. H. Kim, "Silicon photonic receiver and transmitter operating up to 36 Gb/s for λ~1550 nm," *Opt. Exp.*, vol. 23, pp. 12232–12243, May 2015.

[14] Y. Chen, Z. Wang, X. Fan, H. Wang, and W. Li, "A 38 Gb/s to 43 Gb/s monolithic optical receiver in 65 nm CMOS technology," *IEEE Trans. Circuits Syst. I, Reg. Papers*, vol. 60, no. 12, pp. 3173–3181, Dec. 2013.

[15] Q. Pan, Z. X. Hou, Y. Li, A. W. Poon, and C. P. Yue, "A 0.5-V p-well/deep n-well photodetector in 65-nm CMOS for monolithic 850-nm optical receivers," *IEEE Photon. Technol. Lett.*, vol. 26, no. 12, pp. 1184–1187, Apr. 16, 2014.

[16] S. Assefa, F. Xia, W. M. J. Green, C. L. Schow, A. V. Rylyakov, and Y. A. Vlasov, "CMOS-integrated optical receivers for on-chip interconnects," *IEEE J. Sel. Topics Quantum Electron.*, vol. 16, no. 5, pp. 1376–1385, Sep. 2010.

[17] J. Youn, M. Lee, K. Park, W. Kim, and W. Choi, "Low-power 850 nm optoelectronic integrated circuit receiver fabricated in 65 nm complementary metal–oxide semiconductor technology," *IET Circuits, Devices Syst.*, vol. 9, no. 3, pp. 221–226, May 2015.

[18] C. Liu, J. Guo, L. Yu, J. Li, M. Zhang, H. Li, Y. Shi, and D. Dai, "Silicon/2D-material photodetectors: From near-infrared to mid-infrared," *Light, Sci. Appl.*, vol. 10, no. 1, pp. 1–21, Jun. 2021.

[19] S. Ghosh, A. Biswas, and A. Acharyya, "Optical properties of multiple quantum barrier nano-scale avalanche photo diodes," *Int. J. Nanoparticles*, vol. 12, nos. 1–2, pp. 73–110, 2020.

[20] L. Guo, K. Jiang, X. Sun, Z. Zhang, J. Ben, Y. Jia, Y. Wang, and D. Li, "Multiple-quantum-well-induced unipolar carrier transport multiplication in AlGaN solar-blind ultraviolet photodiode," *Photon. Res.*, vol. 9, no. 10, p. 1907, 2021.

[21] S. Ghosh and A. Acharyya, "Multiple quantum barrier nano-avalanche photodiodes—Part I: Spectral response," *Nanosci. Nanotechnol.-Asia*, vol. 9, no. 2, pp. 172–184, Jun. 2019.

[22] V. Fiorentini, F. Bernardini, F. Della Sala, A. Di Carlo, and P. Lugli, "Effects of macroscopic polarization in III-V nitride multiple quantum wells," *Phys. Rev. B, Condens. Matter*, vol. 60, no. 12, pp. 8849–8858, Sep. 1999.

[23] C. E. Dreyer, A. Janotti, C. G. Van de Walle, and D. Vanderbilt, "Correct implementation of polarization constants in Wurtzite materials and impact on III-nitrides," *Phys. Rev. X*, vol. 6, no. 2, Jun. 2016, Art. no. 021038.

[24] S. Ghosh and A. Acharyya, "Multiple quantum barrier nano-avalanche photodiodes—Part II: Excess noise characteristics," *Nanosci. Nanotechnol.-Asia*, vol. 9, no. 2, pp. 185–191, Jun. 2019.

[25] R. Chin, N. Holonyak, G. E. Stillman, J. Y. Tang, and K. Hess, "Impact ionisation in multilayered heterojunction structures," *Electron. Lett.*, vol. 16, no. 12, p. 467, 1980.

[26] G. Yu, G. Wang, H. Ishikawa, M. Umeno, T. Soga, T. Egawa, J. Watanabe, and T. Jimbo, "Optical properties of Wurtzite structure GaN on sapphire around fundamental absorption edge (0.78–4.77 eV) by spectroscopic ellipsometry and the optical transmission method," *Appl. Phys. Lett.*, vol. 70, no. 24, pp. 3209–3211, Jun. 1997.

[27] S. Ghosh and A. Acharyya, "Multiple quantum barrier nano-avalanche photodiodes—Part III: Time and frequency responses," *Nanosci. Nanotechnol.-Asia*, vol. 9, no. 2, pp. 192–197, Jun. 2019.

[28] J. Zheng, L. Wang, X. Wu, Z. Hao, C. Sun, B. Xiong, Y. Luo, Y. Han, J. Wang, H. Li, J. Brault, S. Matta, M. A. Khalfioui, J. Yan, T. Wei, Y. Zhang, and J. Wang, "A PMT-like high gain avalanche photodiode based on GaN/AlN periodically stacked structure," *Appl. Phys. Lett.*, vol. 109, no. 24, Dec. 2016, Art. no. 241105.

[29] A. Acharyya and S. Ghosh, "Dark current reduction in nano-avalanche photodiodes by incorporating multiple quantum barriers," *Int. J. Electron.*, vol. 104, no. 12, pp. 1957–1973, 2017.

[30] A. J. Ekpunobi and A. O. E. Animalu, "Band offsets and properties of AlGaAs/GaAs and AlGaN/GaN material systems," *Superlattices Microstruct.*, vol. 31, no. 5, pp. 247–252, May 2002.

[31] L. Cao, J. Wang, G. Harden, H. Ye, R. Stillwell, A. J. Hoffman, and P. Fay, "Experimental characterization of impact ionization coefficients for electrons and holes in GaN grown on bulk GaN substrates," *Appl. Phys. Lett.*, vol. 112, no. 26, Jun. 2018, Art. no. 262103.

[32] C. Bulutay, "Electron initiated impact ionization in AlGaN alloys," *Semicond. Sci. Technol.*, vol. 17, no. 10, pp. L59–L62, Oct. 2002.

[33] G. R. Li, Z. X. Qin, G. F. Luo, B. Shen, and G. Y. Zhang, "Calculation of the electron and hole impact ionization rate for Wurtzite AlN and GaN," *Semicond. Sci. Technol.*, vol. 25, no. 11, Nov. 2010, Art. no. 115010.

[34] A. Buchner, S. Hadrath, R. Burkard, F. M. Kolb, J. Ruskowski, M. Ligges, and A. Grabmaier, "Analytical evaluation of signal-to-noise ratios for avalanche- and single-photon avalanche diodes," *Sensors*, vol. 21, no. 8, p. 2887, Apr. 2021.

[35] J. G. Graeme, *Photodiode Amplifiers. Op Amp Solutions*. New York, NY, USA: McGraw-Hill, 1996.

[36] D. Wood, *Optoelectronic Semiconductor Devices*. New York, NY, USA: Prentice-Hall, 1994.

[37] A. Acharyya and J. P. Banerjee, "Prospects of IMPATT devices based on wide bandgap semiconductors as potential terahertz sources," *Appl. Nanosci.*, vol. 4, no. 1, pp. 1–14, Jan. 2014.

[38] G. Dong, "Random time response statistics of avalanche photodiodes and its dependence on the mean gain and the impact ionization ratio," Graduate Theses dissertation, Dept. Electro-Optics Photon., Univ. Dayton, Dayton, OH, USA, 1998. [Online]. Available: https://ecommons.udayton.edu/graduate_theses/2386

[39] S. Singh and P. Kumari, "Vertical GaN/InGaN/GaN heterostructure tunnel field-effect transistor: DC and analog/RF performance," *Int. J. Mod. Phys. B*, vol. 37, no. 16, 2023, Art. no. 2350157.

[40] M. Lahrichi, G. Glastre, E. Derouin, D. Carpentier, N. Lagay, J. Decobert, and M. Achouche, "240-GHz gain-bandwidth product back-side illuminated AlInAs avalanche photodiodes," *IEEE Photon. Technol. Lett.*, vol. 22, no. 18, pp. 1373–1375, Sep. 13, 2010.

[41] D. Ji, B. Ercan, G. Benson, A. K. M. Newaz, and S. Chowdhury, "60 A/W high voltage GaN avalanche photodiode demonstrating robust avalanche and high gain up to 525 k," *Appl. Phys. Lett.*, vol. 116, no. 21, May 2020, Art. no. 211102.

[42] Q. Cai, W. K. Luo, Q. Li, M. Li, D. J. Chen, H. Lu, R. Zhang, and Y. D. Zheng, "AlGaN ultraviolet avalanche photodiodes based on a triple-mesa structure," *Appl. Phys. Lett.*, vol. 113, no. 12, Sep. 2018, Art. no. 123503.

[43] L. Gautam, A. G. Jaud, J. Lee, G. J. Brown, and M. Razeghi, "Geiger-mode operation of AlGaN avalanche photodiodes at 255 nm," *IEEE J. Quantum Electron.*, vol. 57, no. 2, pp. 1–6, Apr. 2021.

[44] W. Wang, "Uniform and high gain GaN p-i-n ultraviolet APDs enabled by beveled-mesa edge termination," *IEEE Photon. Technol. Lett.*, vol. 32, no. 21, pp. 1357–1360, Nov. 13, 2020.

[45] F. Jiang and Y. Bu, "GaN/AlN multi-quantumwells infrared detector with short-wave infrared response at room temperature," *Sensors*, vol. 22, p. 4239, Mar. 2022.

[46] Y.-Q. Bie, G. Grosso, M. Heuck, M. M. Furchi, Y. Cao, J. Zheng, D. Bunandar, E. Navarro-Moratalla, L. Zhou, D. K. Efetov, T. Taniguchi, K. Watanabe, J. Kong, D. Englund, and P. Jarillo-Herrero, "A $MoTe_2$-based light-emitting diode and photodetector for silicon photonic integrated circuits," *Nature Nanotechnol.*, vol. 12, no. 12, pp. 1124–1129, Dec. 2017.

[47] P. Ma, N. Flory, Y. Salamin, B. Bäuerle, A. Emboras, A. Josten, T. Taniguchi, K. Watanabe, L. Novotny, and J. Leuthold, "Fast $MoTe_2$ wave guide photodetector with high sensitivity at telecommunication wavelengths," *ACS Photon.*, vol. 5, no. 5, pp. 1846–1852, 2018.

[48] N. Flöry, P. Ma, Y. Salamin, A. Emboras, T. Taniguchi, K. Watanabe, J. Leuthold, and L. Novotny, "Waveguide-integrated van der Waals heterostructure photodetector at telecom wavelengths with high speed and high responsivity," *Nature Nanotechnol.*, vol. 15, no. 2, pp. 118–124, Feb. 2020.

[49] Z. Ma, K. Kikunaga, H. Wang, S. Sun, R. Amin, R. Maiti, M. H. Tahersima, H. Dalir, M. Miscuglio, and V. J. Sorger, "Compact graphene plasmonic slot photodetector on silicon-on-insulator with high responsivity," *ACS Photon.*, vol. 7, no. 4, pp. 932–940, Apr. 2020.

[50] A. Pospischil, M. Humer, M. M. Furchi, D. Bachmann, R. Guider, T. Fromherz, and T. Mueller, "CMOS-compatible graphene photodetector covering all optical communication bands," *Nature Photon.*, vol. 7, no. 11, pp. 892–896, Nov. 2013.

[51] Y. Ding, Z. Cheng, X. Zhu, K. Yvind, J. Dong, M. Galili, H. Hu, N. A. Mortensen, S. Xiao, and L. K. Oxenløwe, "Ultra-compact integrated graphene plasmonic photodetector with bandwidth above 110 GHz," *Nanophotonics*, vol. 9, no. 2, pp. 317–325, Feb. 2020.

[52] X. Gan, R.-J. Shiue, Y. Gao, I. Meric, T. F. Heinz, K. Shepard, J. Hone, S. Assefa, and D. Englund, "Chip-integrated ultrafast graphene photodetector with high responsivity," *Nature Photon.*, vol. 7, no. 11, pp. 883–887, Nov. 2013.

[53] D. Schall, D. Neumaier, M. Mohsin, B. Chmielak, J. Bolten, C. Porschatis, A. Prinzen, C. Matheisen, W. Kuebart, B. Junginger, W. Templ, A. L. Giesecke, and H. Kurz, "50 GBit/s photodetectors based on wafer-scale graphene for integrated silicon photonic communication systems," *ACS Photon.*, vol. 1, no. 9, pp. 781–784, Sep. 2014.

[54] Y. Gao, G. Zhou, N. Zhao, H. K. Tsang, and C. Shu, "High-performance chemical vapor deposited graphene-on-silicon nitride wave guide photodetectors," *Opt. Lett.*, vol. 43, no. 6, pp. 1399–1402, 2018.

[55] R.-J. Shiue, Y. Gao, Y. Wang, C. Peng, A. D. Robertson, D. K. Efetov, S. Assefa, F. H. L. Koppens, J. Hone, and D. Englund, "High-responsivity Graphene–Boron nitride photodetector and autocorrelator in a silicon photonic integrated circuit," *Nano Lett.*, vol. 15, no. 11, pp. 7288–7293, Nov. 2015.

[56] S. Schuler, D. Schall, D. Neumaier, L. Dobusch, O. Bethge, B. Schwarz, M. Krall, and T. Mueller, "Controlled generation of a p-n junction in a waveguide integrated graphene photodetector," *Nano Lett.*, vol. 16, no. 11, pp. 7107–7112, 2016.

[57] S. Schuler, D. Schall, D. Neumaier, B. Schwarz, K. Watanabe, T. Taniguchi, and T. Mueller, "Graphene photodetector integrated on a photonic crystal defect waveguide," *ACS Photon.*, vol. 5, no. 12, pp. 4758–4763, Dec. 2018.

[58] J. E. Muench, A. Ruocco, M. A. Giambra, V. Miseikis, D. Zhang, J. Wang, H. F. Y. Watson, G. C. Park, S. Akhavan, V. Sorianello, M. Midrio, A. Tomadin, C. Coletti, M. Romagnoli, A. C. Ferrari, and I. Goykhman, "Waveguide-integrated, plasmonic enhanced graphene photodetectors," *Nano Lett.*, vol. 19, no. 11, pp. 7632–7644, Nov. 2019.

[59] S. Schuler, J. E. Muench, A. Ruocco, O. Balci, D. van Thourhout, V. Sorianello, M. Romagnoli, K. Watanabe, T. Taniguchi, I. Goykhman, A. C. Ferrari, and T. Mueller, "High-responsivity graphene photodetectors integrated on silicon microring resonators," 2020, *arXiv:2007.03044*.

[60] S. Marconi, M. A. Giambra, A. Montanaro, V. Mišeikis, S. Soresi, S. Tirelli, P. Galli, F. Buchali, W. Templ, C. Coletti, V. Sorianello, and M. Romagnoli, "Photo thermal effect graphene detector featuring 105 Gbit s^{-1} NRZ and 120 Gbit s^{-1} PAM4 direct detection," *Nature Commun.*, vol. 12, no. 1, p. 806, Feb. 2021.

[61] V. Mišeikis, S. Marconi, M. A. Giambra, A. Montanaro, L. Martini, F. Fabbri, S. Pezzini, G. Piccinini, S. Forti, B. Terrés, I. Goykhman, L. Hamidouche, P. Legagneux, V. Sorianello, A. C. Ferrari, F. H. L. Koppens, M. Romagnoli, and C. Coletti, "Ultrafast, zero-bias, graphene photodetectors with polymeric gate dielectric on passive photonic waveguides," *ACS Nano*, vol. 14, no. 9, pp. 11190–11204, Sep. 2020.

[62] Y. Gao, G. Zhou, H. K. Tsang, and C. Shu, "High-speed van der Waals heterostructure tunneling photodiodes integrated on silicon nitride waveguides," *Optica*, vol. 6, no. 4, p. 514, 2019.

[63] X. Wang, Z. Cheng, K. Xu, H. K. Tsang, and J.-B. Xu, "High-responsivity graphene/silicon-heterostructure waveguide photodetectors," *Nature Photon.*, vol. 7, no. 11, pp. 888–891, Nov. 2013.

[64] T. Li, D. Mao, N. W. Petrone, R. Grassi, H. Hu, Y. Ding, Z. Huang, G.-Q. Lo, J. C. Hone, T. Low, C. W. Wong, and T. Gu, "Spatially controlled electrostatic doping in graphene p-i-n junction for hybrid silicon photodiode," *NPJ 2D Mater. Appl.*, vol. 2, no. 1, p. 36, Nov. 2018.

[65] J. S. Guo, J. Li, C. Liu, Y. Yin, W. Wang, Z. Ni, Z. Fu, H. Yu, Y. Xu, Y. Shi, Y. Ma, S. Gao, L. Tong, and D. Dai, "High-performance silicon-graphene hybrid plasmonic wave guide photodetectors beyond 1.55 μm," *Light, Sci. Appl.*, vol. 9, p. 29, Jan. 2020.

[66] Y. L. Yin, "High-speed and high-responsivity hybrid silicon/black-phosphorus wave guide photodetectors at 2 μm," *Laser Photon. Rev.*, vol. 13, no. 6, 2019, Art. no. 1900032.

[67] L. Huang, B. Dong, X. Guo, Y. Chang, N. Chen, X. Huang, W. Liao, C. Zhu, H. Wang, C. Lee, and K.-W. Ang, "Waveguide-integrated black phosphorus photodetector for mid-infrared applications," *ACS Nano*, vol. 13, no. 1, pp. 913–921, Jan. 2019.

[68] Y. Ma, B. Dong, J. Wei, Y. Chang, L. Huang, K. Ang, and C. Lee, "High-responsivity mid-infrared black phosphorus slow light waveguide photodetector," *Adv. Opt. Mater.*, vol. 8, no. 13, Jul. 2020, Art. no. 2000337.

[69] S. Lukman, L. Ding, L. Xu, Y. Tao, A. C. Riis-Jensen, G. Zhang, Q. Y. S. Wu, M. Yang, S. Luo, C. Hsu, L. Yao, G. Liang, H. Lin, Y.-W. Zhang, K. S. Thygesen, Q. J. Wang, Y. Feng, and J. Teng, "High oscillator strength interlayer excitons in two-dimensional heterostructures for mid-infrared photodetection," *Nature Nanotechnol.*, vol. 15, no. 8, pp. 675–682, Aug. 2020.

[70] S. Yuan, R. Yu, C. Ma, B. Deng, Q. Guo, X. Chen, C. Li, C. Chen, K. Watanabe, T. Taniguchi, F. J. García de Abajo, and F. Xia, "Room temperature graphene mid-infrared bolometer with a broad operational wavelength range," *ACS Photon.*, vol. 7, no. 5, pp. 1206–1215, May 2020.

SOMRITA GHOSH received the B.Tech. and M.Tech. degrees in electronics and communication engineering. She is currently pursuing the Ph.D. degree with the Department of Mining Engineering, Kazi Nazrul University, Asansol, West Bengal, India.

ARITRA ACHARYYA was born in 1986. He received the B.E. degree from IIEST, Shibpur, India, in 2007, and the M.Tech. and Ph.D. degrees from the Institute of Radio Physics and Electronics, University of Calcutta, India, in 2010 and 2016, respectively. He is currently an Assistant Professor with the Department of Electronics and Communication Engineering, Cooch Behar Government Engineering College, Harinchawra, West Bengal, India. He has published 92 research papers in peer-reviewed national and international journals, 70 research papers in national and international conference proceedings, and several book chapters. He also authored and edited seven and five number of books, respectively. His research interests include high frequency semiconductor devices, nano-structures, semiconductor physics, transport phenomena, quantum mechanics, and optoelectronics.

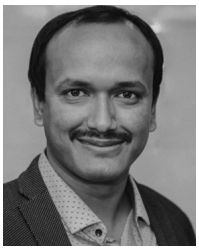

ARINDAM BISWAS received the M.Tech. degree in radio physics and electronics from the University of Calcutta, India, in 2010, and the Ph.D. degree from NIT Durgapur, in 2013. He was a Postdoctoral Researcher with Pusan National University, South Korea, with the prestigious BK21PLUS Fellowship, South Korea. He was a DST-JSPS Invitation Fellow with RIE, Japan; a DST-ASEAN Invitation Fellow with Duy Tan University, Vietnam, and Taylors University, Malaysia; a Visiting Fellow with the Department of Electrical and Computer Engineering, National University of Singapore. He was an Associate Professor (Visiting) with the Research Institute of Electronics, Shizuoka University, Japan. He is currently an Associate Professor with the School of Mines and Metallurgy, Kazi Nazrul University, West Bengal, India, where he has been actively engaged in teaching, research, and administration. He has 53 technical articles in different journals and 55 conference proceedings, eight authored books, 18 edited volumes, and ten book chapters of international repute. He has received research grants from different funding agencies, namely, SERB, DST-ASEAN, DST-JSPS, and UGC. He has also received international research grant from the Centre of Biomedical Engineering, Tokyo Medical and Dental University, in association with RIE, Shizuoka University, Japan, for four consecutive years, from 2019 to 2023. He has supervised six Ph.D. students till date. His research interests include carrier transport in low dimensional system and electronic devices, non-linear optical communication, THz semiconductor source, the IoT, and optimization. He is a Life Member of the Institute of Engineers, India, MGMI, and a regular fellow of the Optical Society of India. He was a reviewer for reputed journals. He has been selected for the IE (I) Young Engineer Award, from 2019 to 2020, the KNU Best Researcher Award (Engineering and Technology), in 2021, the KNU Best Faculty Award 2022 (Faculty of Science and Technology), and the Best Paper Award in different international conferences. He has organized and chaired different international conferences in India and abroad.

AMIT BANERJEE received the Ph.D. degree in semiconductor technology from the Energy Research Unit, Indian Association for the Cultivation of Science, Government of India. In 2016, he joined the Advanced Device Research Division, Research Institute of Electronics, Shizuoka University, National University Corporation, Japan, as a Scientific Researcher. He was also a part of the Innovative Photonics Evolution Research Center, Hamamatsu, Japan. Later, he joined the Microelectronic Technologies and Devices, Department of Electrical and Computer Engineering, National University of Singapore, as a Scientist, in 2017. He moved to India during the Covid'19 global pandemic, in 2020, and currently leading the Microsystem Design-Integration Laboratory, Department of Physics, Bidhan Chandra College with DST/GoI sponsored projects. He is a member of more than 40 international advisory boards with global MNCs, deep-tech startups, technical program committees, in various countries as a Science and Technology Advisor and an Instrumentation and System Architect in microelectronic technologies and devices. He has extensively worked on design and development of high vacuum plasma CVD reactors, which are used in industrial manufacturing of solar cells, coatings, and TFTs. He also developed low cost high vacuum MW-PECVD units, and conceived the process for cost effective commercial grade antireflection coatings (ARC) synthesis for solar cells by nanocrytalline diamonds (NCDs). His current work is on Terahertz Technology, including THz sensors and sources, design, fabrication, aiming at biomedical imaging applications. His recent work on on-chip integrable terahertz detector arrays, are compatible with the state-of-the-art medium-scale semiconductor device fabrication processes, and technologically competitive as on-chip integrable detector arrays for terahertz imaging. He has coauthored more than 50 peer-reviewed scientific papers, presented in more than 30 international conferences as a keynote speaker, received eight international awards, and has authored/edited nine books.

HIROSHI INOKAWA (Member, IEEE) received the Ph.D. degree in electrical engineering from Kyoto University, Kyoto, Japan, in 1985. In 1985, he joined Atsugi Electrical Communications Laboratories, Nippon Telegraph and Telephone Corporation (NTT), Kanagawa, Japan. Since then, he has been engaged in the research and development of scaled-down CMOS devices and silicon single-electron devices. From 2002 to 2018, he was a Researcher with the National Institute of Science and Technology Policy (NISTEP). In 2006, he became a Professor with the Research Institute of Electronics, Shizuoka University, Hamamatsu, Japan, where he has been studying nanodevices for advanced circuits and systems. He is a member of the Japan Society of Applied Physics (JSAP), the Institute of Electronics, Information and Communication Engineers of Japan (IEICE), and the Institute of Electrical Engineers of Japan (IEEJ). He has served as a JSAP Board Member (Representative), from 2001 to 2003, an Editor for *Japanese Journal of Applied Physics*, from 2007 to 2013, and the Chair for the IEEJ Survey Committee of Silicon Nanosystem Integration Technology, from 2009 to 2011.

HIROAKI SATOH (Member, IEEE) received the B.E. degree from the Muroran Institute of Technology, Hokkaido, Japan, in 1999, and the M.E. and Ph.D. degrees from Hokkaido University, Hokkaido, in 2001 and 2004, respectively. From 2004 to 2007, he was a Research Associate with the University of Tokushima, Tokushima, Japan. He was an Assistant Professor and an Associate Professor with the Research Institute of Electronics, Shizuoka University, Hamamatsu, Japan, from 2007 to 2023. His current research interests include computational electromagnetics and its application to silicon nanodevices for advanced photonics. He is a member of the Japan Society of Applied Physics, the Institute of Electronics, Information and Communication Engineers, Japan, and the Institute of Electrical Engineers of Japan.

ALEXEY Y. SETEIKIN is currently the Head of the Computational Biophysics Group, Amur State University, Blagoveshchensk, Russia, and Immanuel Kant Baltic Federal University, Kaliningrad, Russia. His scientific background is in the field of laser-tissue interaction and biophysics. He has the experience in national and international collaboration in the fields of physical and life science research. He is an Editorial Board Member of *Optics and Photonics Journal*.

I. G. SAMUSEV is currently a Professor with the Research and Education Center for Laser Nanotechnology and Information Biophysics, Immanuel Kant Baltic Federal University, Kaliningrad, Russia.